Influence of the Atlantic and Pacific Multidecadal Variability on Arctic Sea Ice in Pacemaker Simulations during 1920–2013

ZHAOXIANGRUI HE,[a] AIGUO DAI,[a] BRIAN E. J. ROSE,[a] AND MATHIAS VUILLE[a]

[a] *Department of Atmospheric and Environmental Sciences, University at Albany, State University of New York, Albany, New York*

(Manuscript received 30 August 2023, in final form 29 April 2024, accepted 15 May 2024)

ABSTRACT: The Atlantic multidecadal variability (AMV) and Pacific multidecadal variability (PMV) can influence Arctic sea ice and modulate its trend, but to what extent the AMV and PMV can affect Arctic sea ice and which processes are dominant are not well understood. Here, we analyze the Community Earth System Model, version 1, idealized and time-varying pacemaker ensemble simulations to investigate these issues. These experiments show that the sea ice concentration varies mainly over the marginal Arctic Ocean, while the sea ice thickness variations occur over the entire Arctic Ocean. The internal components of AMV and PMV can enhance or weaken the decadal sea ice loss rates over the marginal Arctic Ocean by more than 50%. The AMV- or PMV-induced anomalous atmospheric energy transport and downward longwave radiation related to low clouds (thermodynamical processes) and sea ice motion (dynamical processes) contribute to the Arctic surface air temperature and sea ice concentration and thickness changes. Anomalous oceanic heat flux is mainly a response to rather than a cause of sea ice variations. The dynamic processes contribute to the winter Arctic sea ice variations as much as the thermodynamic processes, but they contribute less (more) to the summer Arctic sea ice variability than the thermodynamic processes over the marginal Arctic Ocean (parts of the central Arctic Ocean). Sea ice loss enhances air–sea heat fluxes, which cause oceanic heat convergence and warm near-surface air and the lower troposphere, which in turn melt more sea ice.

KEYWORDS: Arctic; Sea ice; Ice loss/growth; Ice thickness; Climate models; Multidecadal variability

1. Introduction

Arctic sea ice is an important component of the climate system, and its rapid loss is a key indicator of global warming. Satellite observations show rapidly shrinking Arctic sea ice extent since 1979 (Serreze et al. 2007; Comiso et al. 2008; Parkinson 2014; Lindsay and Schweiger 2015; Walsh et al. 2017; Kwok 2018; Onarheim et al. 2018; Schweiger et al. 2019; Brennan et al. 2020; Cai et al. 2021). Climate models project that Arctic sea ice cover will continue to decline in response to anthropogenic forcing (Serreze et al. 2007; Boé et al. 2009; Massonnet et al. 2012; Wang and Overland 2009, 2012; Notz and Stroeve 2016; Notz and SIMIP Community 2020). The decline is especially large in September, as the central Arctic Ocean could be ice-free in September within a few decades (Wang and Overland 2012; Notz and SIMIP Community 2020). Global warming also amplifies the seasonal cycle of Arctic sea ice cover since 2007 (Livina and Lenton 2013). Moreover, the Arctic sea ice loss can further amplify Arctic warming (mainly in the cold season) through the ice–albedo feedback during the warm season (Screen and Simmonds 2010) and enhanced winter oceanic heat and moisture release that warms the overlying atmosphere (Dai et al. 2019; Jenkins and Dai 2021; Deng and Dai 2022), thereby exacerbating sea ice loss.

Some studies have detected signals of human influence in recent Arctic sea ice decline using observations and model ensemble simulations (e.g., Min et al. 2008; Notz and Marotzke 2012; Kirchmeier-Young et al. 2017; Mueller et al. 2018). However, climate models underestimate Arctic sea ice loss in recent decades (Stroeve et al. 2007, 2012; Wang and Overland 2009, 2012; Swart et al. 2015), which implies that internal climate variability may have contributed to the decline. Model results of Kay et al. (2011) suggest that internal variability may have contributed 40%–50% to the Arctic September sea ice loss from 1979 to 2005, with anthropogenic forcing accounting for the rest. Song et al. (2016) reached a similar conclusion by comparing the Arctic sea ice extent trend in the unforced and forced phase 5 of the Coupled Model Intercomparison Project (CMIP5) simulations. Based on reanalysis and model simulations, Ding et al. (2017, 2019) suggested that atmospheric variability over the Arctic might be responsible for 30%–50% of the Arctic September sea ice extent decline since 1979. England et al. (2019) used the Community Earth System Model, version 1 (CESM1), Large Ensemble (CESM1-LE) and CMIP5 simulations to show that internal variability contributed to more than 60% of the August–September sea ice loss during 1958–2017 over the Kara, Laptev, East Siberian, Chukchi, and Beaufort Seas, as well as more than 90% of the April–May sea ice loss during 1958–2017 over the Barents and Greenland Seas. However, recent studies (e.g., Bonan et al. 2021; Kim et al. 2023; Topál and Ding 2023) show that model biases (e.g., in present-day climatology of Arctic sea ice area and sensitivity of the Arctic cryosphere to greenhouse gases and atmospheric circulation) are the primary contributor to the uncertainties in projections of future Arctic sea ice area.

The outstanding question is what has caused internal climate multidecadal variations. In models, some of the internal climate variability is due to intrinsic atmospheric or terrestrial variability unrelated to oceanic influence (Fig. 1 of Lehner and Deser 2023), while the rest (especially low-frequency

Corresponding author: Zhaoxiangrui He, hzxrkb@gmail.com

DOI: 10.1175/JCLI-D-23-0520.1

variability) originates from the oceans. Yu et al. (2017) showed that the leading mode of the empirical orthogonal function (EOF) of the observed Arctic and Antarctic sea ice concentration (SIC) during 1979–2013 is positively correlated with the Atlantic multidecadal variability (AMV) but negatively correlated with the Pacific multidecadal variability (PMV). Meehl et al. (2018) used an atmospheric model forced with a negative (positive) convective heating anomaly in the tropical Pacific (Atlantic) to show that the cold (warm) phase PMV (AMV) might have accelerated the Arctic sea ice loss during 2000–14. These results imply that the AMV and PMV may have contributed to recent Arctic sea ice changes.

The PMV is a decadal-to-multidecadal mode of variability in Pacific sea surface temperature (SST), whose spatial pattern is similar to El Niño–Southern Oscillation (ENSO) but has larger (smaller) SST variations in the extratropical (tropical) Pacific (Dong et al. 2018). Recent PMV in observations since 1920 is mostly internally generated, although external forcing may have contributed to the PMV since the early 1990s (Hua et al. 2018). The PMV tends to reside in its warm (cold) phase in response to greenhouse gas (aerosol) forcing (Smith et al. 2016; Heede and Fedorov 2021; Wills et al. 2022). The warm-phase PMV strengthens the Aleutian low and induces anomalous northerly winds over the Bering Sea, which advect cold air from the Arctic to lower latitudes and hence cool the low-level air over the Bering Sea and increase sea ice cover in this region (Screen and Francis 2016; X.-Y. Yang et al. 2020). It also weakens the polar vortex, which leads to subsidence warming and enhanced downward longwave (LW) radiation and thus sea ice reduction over the rest of the Arctic (Liu et al. 2021; Svendsen et al. 2021). Observations and model simulations show that Arctic warming in response to Arctic sea ice loss is greater during PMV's cold phase than during its warm phase (Screen and Francis 2016). X.-Y. Yang et al. (2020) also noted that in satellite data Bering Sea spring ice cover expands (declines) during the warm (cold) PMV phase. Summer sea ice loss in the western Arctic (70°–81.5°N, 130°W–180°) from 1979 to 2016 is highly correlated with the Pacific North America (PNA) pattern (Liu et al. 2021), which is a Northern Hemisphere midlatitude climate mode closely related to ENSO and PMV (Horel and Wallace 1981). Liu et al. (2021) suggested that the PNA-induced increases in heat and moisture transport into the western Arctic could change the lower-troposphere temperature, specific humidity, cloud cover, and downwelling LW radiation over the western Arctic, which could enhance sea ice decline there. Svendsen et al. (2021) found that the PMV contributed up to 50% of the decadal Arctic surface air temperature trends during the twentieth century. They also proposed that the ocean heat transport from the Atlantic to the Arctic can modulate the influence of PMV on Arctic temperature. In addition, Screen and Deser (2019) used the CESM1-LE to show that Arctic sea ice loss is faster than the man-made decline when the PMV shifts from a cold phase to a warm phase and the opposite is also true.

The AMV is the multidecadal mode in North Atlantic SST with a horseshoe pattern of warmer (cooler) SST over the North Atlantic during its warm (cold) phase (Zhang et al. 2019). Decadal variations in volcanic and anthropogenic aerosols have likely contributed substantially to recent AMV since 1920 (Qin et al. 2020a,b; He et al. 2023). The warm-phase AMV decreases sea level pressure (SLP) and anticyclone frequency over the Arctic Ocean, which results in increased low-level cloud cover and downwelling LW radiation and hence reduces sea ice (Castruccio et al. 2019). It also affects sea ice by altering two wind-driven ice drift patterns: the Beaufort Gyre and the Transpolar Drift Stream (Castruccio et al. 2019). Chylek et al. (2009, 2010) noted the in-phase relationship between Arctic temperature and the AMV index and suggested that the AMV contributes to Arctic air temperature variability on multidecadal time scales. A 1000-yr control simulation shows that the AMV and the Atlantic meridional overturning circulation, which are closely related (Zhang et al. 2019), are anticorrelated with Arctic sea ice extent, thickness, and concentration, especially during boreal winter (Mahajan et al. 2011). Day et al. (2012) attributed up to 30% (70%) of the September (March) Arctic sea ice extent decline from 1979 to 2010 to the AMV. Zhang (2015) used a multiple regression model to quantify the contributions of the anomalous Atlantic and Pacific meridional heat transport to summer Arctic sea ice variability in a 3600-yr control simulation. The results suggest that Atlantic heat transport into the Arctic contributes significantly to the September Arctic sea ice multidecadal variations. On the other hand, Castruccio et al. (2019) analyzed pacemaker simulations from three models to show that the warm-phase AMV reduces Arctic sea ice thickness and concentration mainly through atmospheric teleconnections.

The AMV and PMV influence Arctic sea ice through perturbations in the atmosphere and oceans. The atmospheric perturbation affects Arctic sea ice through thermodynamic effects on ice melting and dynamic effects on ice drift (Polyakov et al. 2012; Döscher et al. 2014). The thermodynamic effects include the direct effect of radiative and turbulent surface fluxes and the indirect effect of precipitation and clouds, which could influence surface albedo and radiative fluxes (Döscher et al. 2014). The dynamic effects are related to the AMV- and PMV-induced wind anomalies, which affect wind-driven currents and thus sea ice drift (Vihma et al. 2012). In addition, the oceanic perturbation affects Arctic sea ice through heat and salinity transported in and out of the Arctic (Mahajan et al. 2011; Zhang 2015).

The abovementioned studies explain how the AMV and PMV influence Arctic sea ice in several ways. However, our understanding of how multidecadal variability affects Arctic sea ice area and volume is limited by the lack of sea ice observations before the satellite era (i.e., prior to 1979). Coupled model simulations can be helpful for studying the impacts of multidecadal variability on Arctic sea ice. Pacemaker simulations are coupled global climate model simulations, except for specific domains in one ocean basin, where SSTs are prescribed. Castruccio et al. (2019) showed that such simulations are capable of accurately reproducing the response of Arctic sea ice to Atlantic SST variations and the observed atmosphere–ocean–ice interactions. Here, we attempt to use the AMV/Atlantic and PMV/Pacific pacemaker ensemble simulations to quantitatively estimate the effects of the AMV and PMV

on recent Arctic sea ice loss and examine the processes considered in the literature to determine their relative roles. Specifically, we analyze the changes in Arctic SIC and sea ice thickness (SIT) and related atmospheric and oceanic fields in two types of pacemaker simulations performed by the National Center for Atmospheric Research (NCAR) using the CESM1 (Ruprich-Robert et al. 2017; Meehl et al. 2021). We estimate how much the internal components of AMV and PMV could affect Arctic sea ice area and volume and modulate recent Arctic sea ice loss rates; reveal the dominant processes through which the AMV and PMV influence Arctic sea ice; and analyze atmosphere–ocean–ice feedbacks in these processes. Our results should help adjust the Arctic sea ice loss trend in model projections with anthropogenic forcing by taking the contributions of the AMV and PMV into consideration and providing evidence for the hypothesis that the AMV and PMV contribute to the varying Arctic sea ice loss rates during 1920–2013. Section 2 describes the data and methods used here. Section 3 presents the results, and section 4 summarizes and discusses the main results.

2. Data and methods

a. *Idealized pacemaker simulations*

To investigate how the AMV and PMV influence Arctic sea ice concentration and thickness, we first analyzed monthly data from idealized pacemaker simulations, which use fixed monthly SST anomaly (SSTA) patterns of the AMV or PMV over their respective region, while keeping the model fully coupled over the rest of the globe under preindustrial forcing. Please note that the model used its own SST climatology. NCAR used the CESM1 (Hurrell et al. 2013) to run 30-member warm-phase AMV and 30-member cold-phase AMV pacemaker simulations (Ruprich-Robert et al. 2017; Castruccio et al. 2019) and 10-member warm-phase PMV and 10-member cold-phase PMV pacemaker simulations (Meehl et al. 2021). Each simulation has nominal 1° × 1° horizontal grids and is run for 10 years with the external forcings held constant at preindustrial values. In these simulations, the seasonal cycle of the AMV or PMV SSTA patterns is prescribed over 8°–65°N in the North Atlantic (the fully restored SST anomalies are linearly damped to 0 in 8° buffer zones at the southern and northern boundaries) or 40°S–60°N in the Pacific and kept constant in time, while the rest of the model is fully coupled. The SSTA patterns of AMV and PMV are obtained by regressing the residuals of the observed SST at each grid point (i.e., subtracting the first EOF component of the global SST field, which is an estimate of the externally forced component of SST, from the SST time series) onto the internal components of AMV and PMV indices defined by NCAR (Meehl et al. 2021). The SST data are from the Extended Reconstructed Sea Surface Temperature, version 3 (ERSST.v3; Smith et al. 2008). The SSTA difference over the North Atlantic between the warm-phase AMV and cold-phase AMV experiments is about 0.3°C (Fig. A1a), and the SSTA difference over the eastern tropical Pacific between the warm-phase PMV and cold-phase PMV experiments is about 0.5°C (Fig. A1b; see the appendix).

b. *Time-varying pacemaker simulations*

To study the impacts of AMV and PMV on Arctic sea ice in a more realistic fashion, we also analyzed monthly data from time-varying pacemaker experiments, which were performed by NCAR using CESM1. The Pacific pacemaker ensemble consists of 20-ensemble-member runs at approximately 1° horizontal grid spacing (Deser et al. 2017). Each simulation is nudged to observed time-varying SSTA (from ERSST.v3b) from 1920 to 2013 in the eastern tropical Pacific (15°S–15°N, 180°–American Coast) with two linear buffer belts along 15°–20°S and 15°–20°N. The fully nudged SST anomalies are gradually damped to 0 in the buffer zones. The rest of the globe is fully coupled in the simulations. The radiative forcing scenario from 1920 to 2005 is based on the historical forcing used in CMIP5 experiments, while from 2006 to 2013 it is based on the representative concentration pathway 8.5 (RCP8.5) (Moss et al. 2010). The model and external forcing are the same as in the CESM1-LE experiments (Kay et al. 2015), except for ozone forcing. The CESM1-LE includes 40 members of fully coupled CESM1 simulations from 1920 to 2100. Each member has the same radiative forcing scenario, with historical forcing during 1920–2005 and RCP8.5 during 2006–2100.

The Atlantic pacemaker ensemble consists of 10 ensemble members (D. Yang et al. 2020). In each simulation, the time-evolving SST anomalies in the North Atlantic (5°–55°N) are nudged to observations from ERSST.v3b during 1920–2013, with two linear buffer zones along 0°–5°N and 55°–60°N. The rest of the model is fully coupled. The model and external forcing are the same as in the Pacific pacemaker ensemble.

The Pacific SST response to AMV is weaker in the time-varying Atlantic than in the idealized AMV pacemaker simulations, especially in the tropical and northeastern Pacific (Figs. A1a,c), which may lead to different Arctic responses in the two types of AMV/Atlantic pacemaker simulations as the concurrent SST anomalies in the other basin can also have significant impacts on Arctic climate. Comparisons with observations seem to suggest that the response patterns from the idealized AMV pacemaker simulations may be more realistic than the time-varying Atlantic pacemaker runs (Meehl et al. 2021). In contrast, the SSTA patterns in the idealized PMV and time-varying Pacific pacemaker ensembles are similar to each other (Figs. A1b,d), which explains why the Arctic climate responses in the two types of PMV/Pacific pacemaker simulations generally agree with each other.

The CESM1 can produce the observed AMV phases and SSTA pattern of PMV realistically over the period 1920–2005 (Wang and Miao 2017; Murphy et al. 2021) and reproduce the periodicity of PMV (Wang et al. 2015). The CESM1 captures the observed spatiotemporal characteristics of AMV and its impacts on global climate reasonably well and more realistically than the fully coupled simulations (e.g., CESM1-LE; Si et al. 2023). The CESM1-simulated Arctic SIC mean patterns are consistent with those from the Met Office Hadley Centre Sea Ice and Sea Surface Temperature dataset, version 1 (HadISST1; Rayner et al. 2003) (Fig. A2), which are SIC analyses that combine numerous sea ice charts, passive microwave

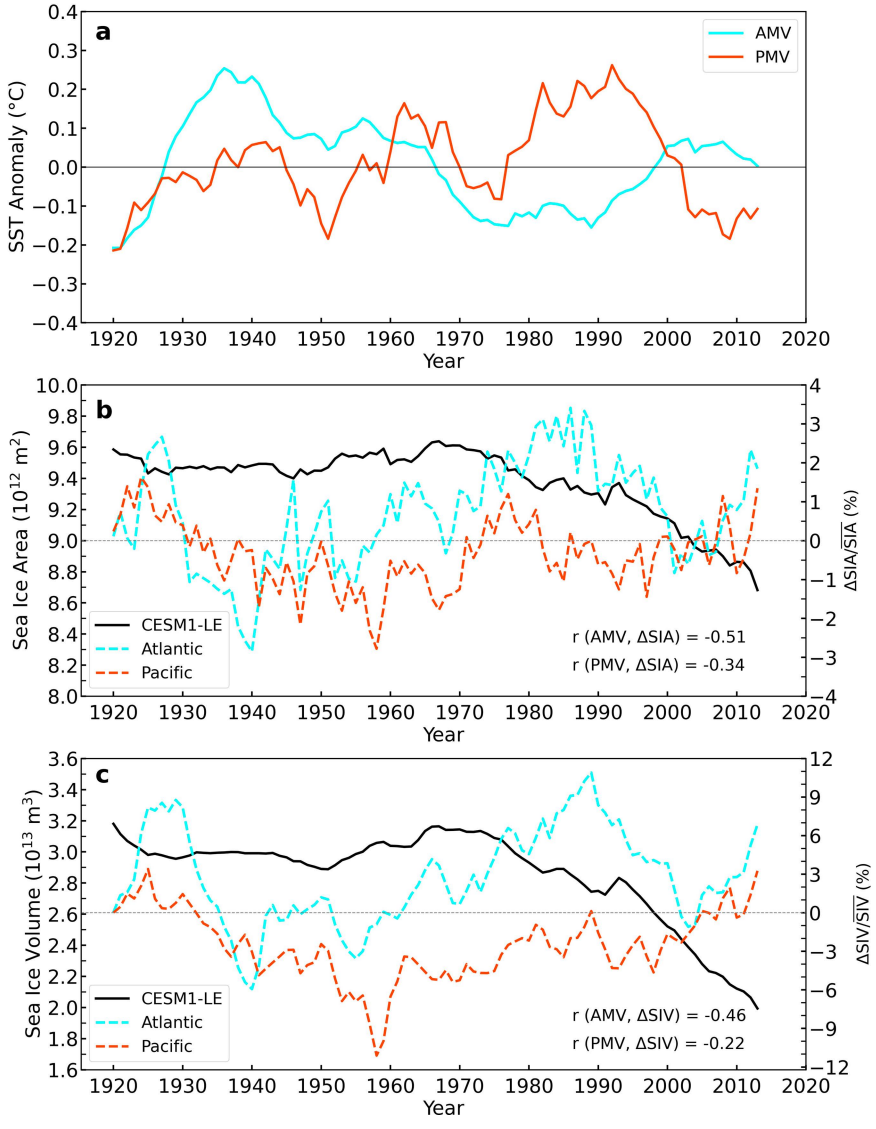

FIG. 1. (a) Time series of the AMV and PMV indices from 1920 to 2013. These indices represent mainly unforced internal variations as the externally forced changes are removed through the CMIP5-based detrending (see section 2c for details). Time series of ensemble means (solid; left y axis) of the annual (unsmoothed) Arctic (66.5°–90°N) mean (b) sea ice area and (c) sea ice volume from the CESM1-LE. The dashed lines (right y axis) show the difference between the ensemble means of the Atlantic/Pacific pacemaker runs and CESM1-LE expressed in percentage of the CESM1-LE mean over 1920–2013. The dashed lines represent the impacts from the internally generated Atlantic and Pacific SST variations. The correlation coefficients between the dashed lines in (b) and (c) and the unsmoothed AMV and PMV indices are shown in the right bottom corner of each panel.

satellite retrievals, and National Centers for Environmental Prediction operational ice analyses.

c. Data analysis

To isolate the influence of the AMV- or PMV-related SST forcing, the ensemble mean of the AMV/Atlantic or PMV/Pacific pacemaker runs was calculated, which should contain reduced random internal variations (reduced by a factor of $1/N^{1/2}$, N being the number of ensemble runs). Thus, the ensemble mean of the idealized PMV (AMV) pacemaker ensemble simulations with $N = 10$ (30) would contain about 32% (18%) of the original internal variability seen in individual runs, while the SST-forced changes would remain, as the SST forcing is identical, and thus, the response is likely similar across all ensemble members. The averaging over the 10-yr integration will further reduce the internal variability, further enhancing the significance of the forced signal. Similarly, the ensemble and temporal/spatial averaging of the time-varying

Pacific (Atlantic) pacemaker simulations with $N = 20$ (10) will substantially reduce the internal variability and keep the common forced signal among the ensemble runs.

In the idealized pacemaker simulations, the ensemble mean of a field (e.g., SIC) for the warm- or cold-phase PMV/AMV simulations largely represents the response of this field to the warm- or cold-phase PMV/AMV plus the mean climatology. The difference in a field between the warm and cold PMV (AMV) ensemble means is used to quantify the impacts of the PMV (AMV) on this field.

In the time-varying pacemaker simulations, averaging a monthly field over the Pacific (Atlantic) ensemble runs yields this field's response to the Pacific (Atlantic) SSTA and external forcing (plus the mean climatology). To obtain the impacts of the warm- or cold-phase PMV (AMV) on this field, first, we subtracted the CESM1-LE ensemble mean of this field from the pacemaker ensemble mean of this field to obtain the unforced internal variability of this field. Second, we smoothed the internal component of the ensemble mean of this field using an 11-yr moving average to obtain the decadal–multidecadal internal variability of this field. Third, we constructed the warm- and cold-phase composites of the decadal–multidecadal internal variations of this field using the PMV (AMV) index. The PMV index is defined as the 11-yr moving-averaged internal component of the observed SSTA from ERSST.v3b averaged over the eastern tropical Pacific (15°S–15°N, 150°–90°W). Following Dai et al. (2015), the forced component in the observed SSTA time series was estimated over 1920–2013 through a linear regression at each grid point against the ensemble mean of global-mean surface air temperature time series from multiple CMIP5 models, which represents the forced signal, and then this forced component was removed from the observed SSTA to derive the internal component. The AMV index is defined as the 11-yr moving-averaged internal component of the SSTA from ERSST.v3b averaged over the North Atlantic (0°–60°N, 80°W–0°). Fourth, this field's response to warm- or cold-phase PMV (AMV) is represented by the average of warm or cold composite of this field, which is calculated by averaging this field over the years when the PMV (AMV) index is larger or smaller than the 1.5 or −1.5 (0.25 or −0.25) standard deviations of the PMV (AMV) index during 1920–2013. The thresholds for the composites are chosen to ensure that the values of the composite means of SSTA from the time-varying runs over the AMV or PMV region match the intensity of those from the idealized pacemaker ensembles (Fig. A1).

d. Energy budgets

To compare the contributions of atmospheric and oceanic processes to sea ice variations, we use energy budgets to analyze the diagnostic variables associated with such processes. Monthly data are used to calculate terms in the energy budgets. The atmospheric energy budget equation at each grid box can be written as (Trenberth 1997; Fasullo and Trenberth 2008a,b)

$$\frac{\partial A_E}{\partial t} + \nabla \cdot \mathbf{F}_A = \mathrm{ASR} - \mathrm{OLR} - \mathrm{SW}^{\downarrow}_{\mathrm{net}} + \mathrm{LW}^{\uparrow}_{\mathrm{net}} + \mathrm{LH} + \mathrm{SH}, \tag{1}$$

where

$$A_E = \frac{1}{g}\int_0^{p_s}\left(C_pT + \frac{1}{2}u^2 + \frac{1}{2}v^2 + Lq + gz\right)dp, \tag{1a}$$

$$\mathbf{F}_A = \frac{1}{g}\int_0^{p_s}\mathbf{v}\left(C_pT + \frac{1}{2}u^2 + \frac{1}{2}v^2 + Lq + gz\right)dp. \tag{1b}$$

In this equation, A_E is the atmospheric energy of the column over the grid box; $\mathbf{F}_A$ is the vertically integrated atmospheric energy horizontal transport or flux; and ∇ is an operator for horizontal divergence. The $\mathbf{v}$ ($=u, v$), T, q, p, p_s, and z are, respectively, atmospheric horizontal winds, temperature, specific humidity, pressure, surface air pressure, and geopotential height. ASR, OLR, $\mathrm{SW}^{\downarrow}_{\mathrm{net}}$, and $\mathrm{LW}^{\uparrow}_{\mathrm{net}}$ denote absorbed shortwave radiation at the top of the atmosphere (TOA), TOA outgoing longwave radiation, surface downward net shortwave radiation (i.e., $\mathrm{SW}^{\downarrow}_{\mathrm{net}}$ is positive downward), and surface upward net longwave radiation (i.e., $\mathrm{LW}^{\uparrow}_{\mathrm{net}}$ is positive upward). LH and SH are surface latent heat flux and sensible heat flux (both positive upward). The standard constants C_p, L, and g correspond to the specific heat of air at constant pressure, latent heat of vaporization of water, and gravitational acceleration at the surface of Earth. We use Eq. (1) to estimate atmospheric energy transport convergence $-\nabla \cdot \mathbf{F}_A$ by writing this equation as

$$-\nabla \cdot \mathbf{F}_A = \frac{\partial A_E}{\partial t} - (\mathrm{ASR} - \mathrm{OLR} - \mathrm{SW}^{\downarrow}_{\mathrm{net}} + \mathrm{LW}^{\uparrow}_{\mathrm{net}} + \mathrm{LH} + \mathrm{SH}). \tag{2}$$

It is important to note that based on Eqs. (1b) and (2), $\mathbf{F}_A$ or $-\nabla \cdot \mathbf{F}_A$ can vary due to changes in either horizontal winds $\mathbf{v}$ (i.e., atmospheric circulation) or atmospheric energy A_E or both. For example, changes in the surface fluxes ($\mathrm{LW}^{\uparrow}_{\mathrm{net}}$ + LH + SH) associated with sea ice variations in winter can greatly alter local A_E, which can result in changes in $\mathbf{F}_A$ or $-\nabla \cdot \mathbf{F}_A$ even without circulation changes. Equation (2) illustrates the impact of these fluxes on $-\nabla \cdot \mathbf{F}_A$, which occurs mainly through their direct impact on local A_E. Thus, a $\mathbf{F}_A$ or $-\nabla \cdot \mathbf{F}_A$ change can result from local flux changes, in which case the concurrent changes in atmospheric winds and/or temperature are likely a response, rather than a cause, of the locally induced $\mathbf{F}_A$ or $-\nabla \cdot \mathbf{F}_A$ change. The same argument also applies to the oceanic heat transport flux $\mathbf{F}_O$ and its convergence ($-\nabla \cdot \mathbf{F}_O$) discussed below.

On time scales relevant to this study, the atmospheric influence on the ocean is mainly limited to the mixed layer. Therefore, we analyzed the mixed layer oceanic energy budget. The oceanic energy budget equation at each ocean grid box can be written as (Trenberth 1997; Fasullo and Trenberth 2008a,b)

$$\frac{\partial O_E}{\partial t} + \nabla \cdot \mathbf{F}_O = F_{\mathrm{net}} + F_D, \tag{3}$$

where

$$O_E = \int_0^D \rho C_w T dz, \text{ and} \tag{3a}$$

$$\mathbf{F}_O = \int_0^D \rho C_w \mathbf{v} T dz. \tag{3b}$$

Here, O_E is the mixed layer oceanic energy, which is estimated using the ocean heat content only, as changes in oceanic kinetic energy and geopotential energy are small. The term $\mathbf{F}_O$ is the vertically integrated ocean mixed layer horizontal heat flux; F_{net} and F_D are the net energy fluxes at the surface and bottom of the mixed layer (F_{net} is positive downward; F_D is positive upward), respectively; and $\mathbf{v}$, T, and D, are, respectively, the ocean horizontal velocity, ocean temperature, and mixed layer depth. The standard constants ρ and C_w correspond to a reference density of seawater and the specific heat of seawater. The tendency of O_E can be further approximated by (Bitz et al. 2012; Roberts et al. 2017; Singh et al. 2017)

$$\frac{\partial O_E}{\partial t} = \rho C_w D \frac{\partial \text{SST}}{\partial t}. \tag{4}$$

Here, we use SST tendency as an approximate measure of the temperature tendency for the ocean mixed layer as the temperature is well mixed in this layer. The ocean mixed layer heat transport convergence in horizontal and vertical directions ($-\nabla \cdot \mathbf{F}_O + F_D$) is estimated using Eq. (3) by writing it as

$$-\nabla \cdot \mathbf{F}_O + F_D = \frac{\partial O_E}{\partial t} - F_{\text{net}}. \tag{5}$$

We do not attempt to isolate separately the horizontal ($-\nabla \cdot \mathbf{F}_O$) and vertical ($F_D$) components of the ocean heat transport convergence into the mixed layer.

e. *Sea ice area tendency terms*

The sea ice component of CESM1 is based on the Community Ice Code (CICE), version 4 (Hurrell et al. 2013). CICE includes two output variables named daidtd and daidtt. The variable daidtd is the SIC tendency due to dynamics/transport, i.e., wind- and current-driven horizontal transport, ridging, and other mechanical processes of sea ice, while daidtt is the SIC tendency due to thermodynamic processes that lead to the growth and melting of sea ice. We analyzed these two variables to quantify the dynamic and thermodynamic contributions to SIC variations.

3. Results

a. *The impacts of AMV and PMV on Arctic sea ice*

Figures 1b and 1c show that the ensemble means of Arctic mean sea ice area and volume in the time-varying Atlantic pacemaker simulations can deviate from the ensemble mean in the CESM1-LE by up to 2.7% of the 1920–2013 mean for certain years (e.g., the 1980s) for sea ice area and 8.3% for sea ice volume. Figure 1 shows that the phase change of AMV from the 1930s (warm phase) to the 1980s (cold phase) led to an anomalous upward trend in Arctic sea ice area and volume, and the transition of AMV phase from the 1980s (cold phase) to the early 2000s (warm phase) accelerated Arctic sea ice loss from 1990 to 2005, which may have contributed to the recent rapid sea ice decline (Day et al. 2012). Arctic mean sea ice area and volume anomalies are negatively correlated with the unsmoothed AMV index during 1920–2013 ($r = -0.51$ and -0.46; Figs. 1b,c). During the recent warm AMV phase from 1999 to 2013, the AMV enhanced the December–February (DJF) and June–August (JJA) sea ice loss over the Greenland Sea by more than 50% compared with the forced trend (whose value is generally negative) and reduced the negative trend over most of the central Arctic Ocean, Chukchi Sea, and East Siberian Sea (Figs. 2a,b). Figures 2c and 2d show that over the period 1989–2008 (i.e., the period that the AMV shifted from its cold phase to its warm phase), the AMV accelerated the SIC decrease by more than 100% (compared to the forced trend) over the Greenland, Barents, Beaufort, and Bering Seas and the Sea of Okhotsk. Day et al. (2012) showed that the contribution of AMV to Arctic sea ice extent changes for the period 1979–2010 is 5%–31% in September and 24%–72% in March. Our results are consistent with Day et al. (2012) but with larger estimates (i.e., 48.8% in JJA and 68.7% in annual mean for the same period). Recently, some studies (e.g., Scaife and Smith 2018; Smith et al. 2019, 2020) discovered that climate models could underestimate the forced response (e.g., the response to prescribed Atlantic or Pacific SSTA in this study) which is referred to as the signal-to-noise paradox, particularly over the North Atlantic. Therefore, our quantitative estimate of the contribution of internal AMV or PMV to variability in Arctic sea ice area or volume might be lower than that in the real world.

The idealized and time-varying Atlantic pacemaker ensembles show consistent changes in Arctic surface air temperature (SAT) and sea ice (Figs. 3a–d). The warm-phase AMV generally warms the Arctic (by 0.2°–0.4°C, relative to the cold phase) except over the Greenland Sea (Figs. 3a,b). The sea ice response is consistent with the temperature response, as indicated by the negative spatial pattern correlations between them. During the AMV warm phase, SIC decreases over Arctic marginal ice zone (MIZ) especially in JJA, except for the Greenland Sea in DJF, and the SIT decreases from the central Arctic to the Pacific sector of the Arctic compared with the AMV cold phase (Figs. 3a,b). One interesting point is that during JJA SIT decreases correspond to SIC decreases over MIZ, where sea ice is thin, whereas the similar SIT decreases correspond to slight SIC decreases over the central Arctic, where sea ice is thick. In the time-varying Atlantic pacemaker simulations, the SAT, SIC, and SIT's responses to the AMV (Figs. 3c,d) are generally consistent with those from the idealized pacemaker simulations (Figs. 3a,b), except that the time-varying Atlantic pacemaker ensemble shows stronger warming and SIC reduction over the Greenland Sea and Barents Sea (Figs. 3c,d). These results agree with previous studies based on fully coupled model simulations and remote sensing observations (Chylek et al. 2009, 2010; Day et al. 2012; Mahajan et al. 2011; Yu et al. 2017; Castruccio et al. 2019). The SIC anomaly patterns in Figs. 3a–d are different from the SIC trend patterns in Figs. 2c and 2d, as the anomalies and trends may have different patterns.

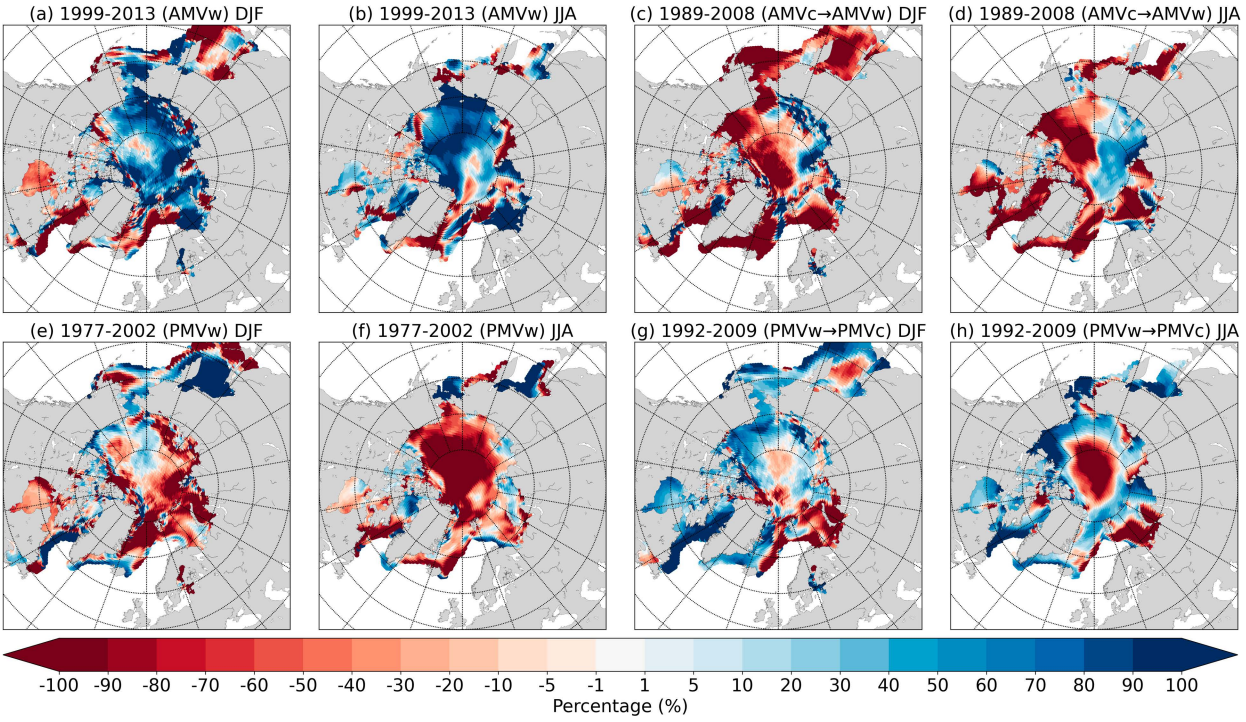

FIG. 2. The difference between the ensemble means of the SIC trend in the time-varying Atlantic pacemaker runs and CESM1-LE expressed as a percentage of the absolute value of the SIC trend in the CESM1-LE mean for the period 1999–2013 for (a) DJF and (b) JJA. (c),(d) As in (a) and (b), but for the period 1989–2008. The difference between the ensemble means of the SIC trend in the time-varying Pacific pacemaker runs and CESM1-LE expressed as a percentage of the absolute value of the SIC trend in the CESM1-LE mean for the period 1977–2002 for (e) DJF and (f) JJA. (g),(h) As in (e) and (f), but for the period 1992–2009. A positive percentage indicates that the forced CESM1-LE trend, which is negative, is weakened by the AMV or PMV, while a negative percentage means that the forced decreasing trend is enhanced by the AMV or PMV.

The spatial anticorrelation between Arctic SAT and SIC or SIT (Figs. 3a–d) is expected as warmer SAT would lead to more ice melting, which could further enhance surface warming through reduced surface albedo in the warm season and a reduced ice insulation effect in the cold season (Dai et al. 2019). Indeed, the winter surface latent and sensible heat flux and upward LW radiation response are anticorrelated spatially with the SIC response over the Arctic, with large upward fluxes over areas with large sea ice loss, such as the Davis Strait, Greenland, Barents–Kara, and Chukchi Seas (Figs. 4a,c). During the cold season, Arctic SAT is much colder than SST, so any open water surfaces would increase surface heat, moisture, and radiative fluxes into the air (Pinto et al. 2003; Dai et al. 2019), while thinner sea ice implies that the heat exchange between the atmosphere and the ocean is less obstructed by the sea ice layer. Thus, the sea ice reduction would increase oceanic heating of the overlying air in winter, leading to SAT increases and warming of the lower troposphere, which would lead to increased downward LW radiation (this could also be caused by increased moisture exchange between the atmosphere and the ocean) and thus more sea ice loss, a positive feedback loop (referred to as the sea ice feedback) described previously (e.g., Deng and Dai 2022; Dai and Jenkins 2023).

The differences in the Arctic sea ice area and sea ice volume between the Pacific pacemaker ensemble and the CESM1-LE can reach 1.4% of the 1920–2013 mean for sea ice area and 7.0% for sea ice volume (Figs. 1b,c), which suggests that the PMV can significantly modulate the externally forced changes in Arctic sea ice on multidecadal time scales. The Arctic sea ice area and volume in the time-varying Pacific pacemaker ensemble are slightly lower than those in the CESM1-LE for most of the period 1930–2013 (Figs. 1b,c). Compared to the correlations between the differences between the Atlantic pacemaker and CESM1-LE and the unsmoothed AMV index, the sea ice area and volume differences between the Pacific pacemaker and CESM1-LE have weaker negative correlations (of -0.34 and -0.22) with the unsmoothed PMV index. This may be due to regionally opposite influences of the PMV on Arctic sea ice. Figures 2e and 2f show that during 1977–2002 (a PMV warm phase), the sea ice loss was enhanced over the Greenland and Barents Seas in both DJF and JJA and over the central Arctic in JJA, but weakened over the Sea of Okhotsk. Figures 2g and 2h show that during 1992–2009 when the PMV shifts from a warm phase to a cold phase, the sea ice loss is reduced over the Labrador, Greenland, Beaufort, Chukchi, and Bering Seas, while it is significantly enhanced over the Barents–Kara Sea in both DJF and JJA and over the central Arctic in JJA.

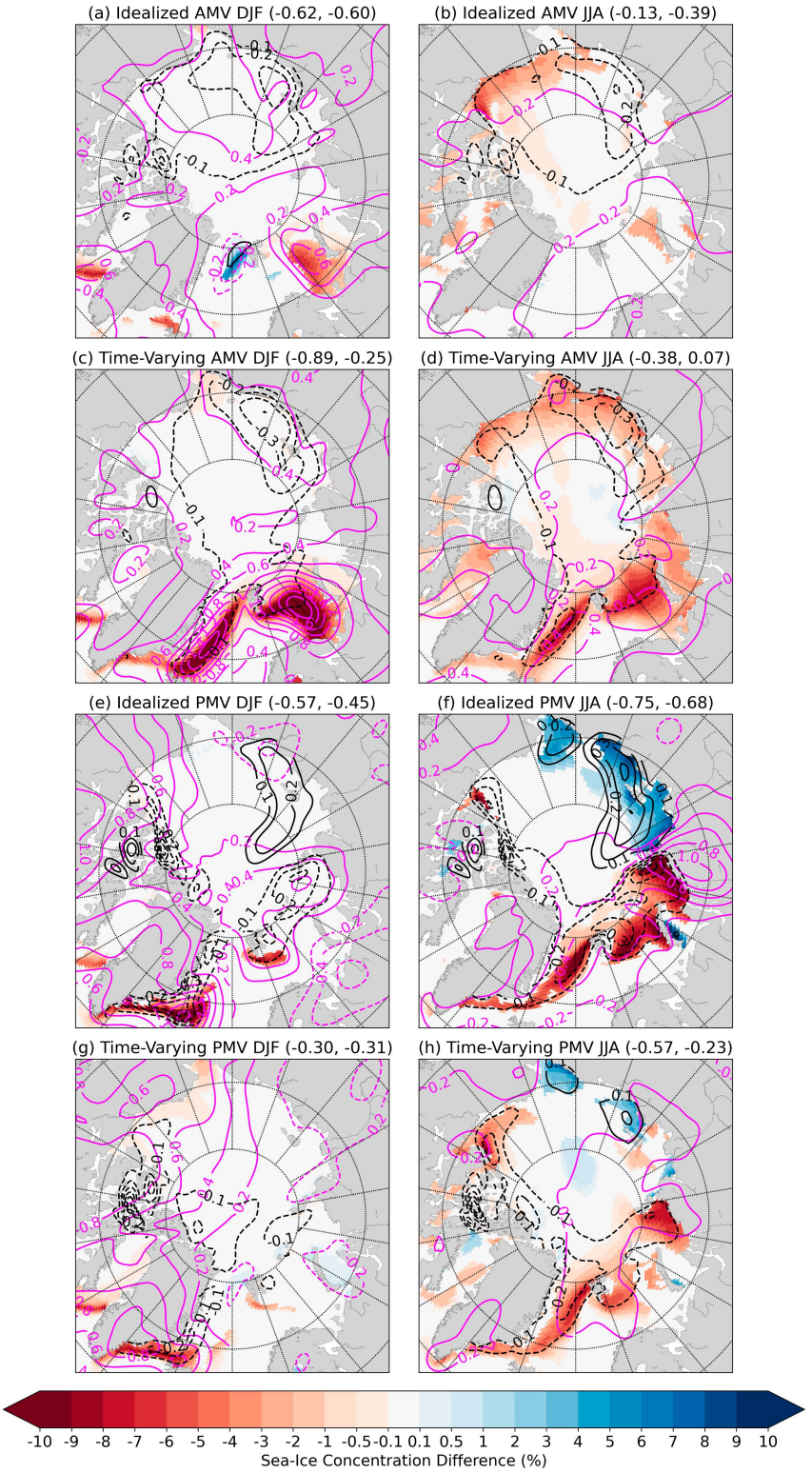

FIG. 3. Differences in the 10-yr averaged ensemble means of (a) DJF and (b) JJA SIC (%; shading), SAT (°C; magenta contours with an interval of 0.2°C), and SIT (m; black contours with an interval of 0.1 m) between the idealized warm- and cold-phase AMV pacemaker simulations. (c),(d) As in (a) and (b), but for the warm-phase minus cold-phase composite differences in the 11-yr moving averaged data from the ensemble mean difference between the

The PMV warm phase cools the East Siberian and southern Barents–Kara Seas and warms other parts of the Arctic Ocean during DJF and warms most of the Arctic during JJA relative to the PMV cold phase (Figs. 3e,f). The sea ice change patterns are consistent with the temperature patterns, as SIC increases over the Chukchi and East Siberian Seas, and Nunavut of Canada in JJA, and declines over the rest of the Arctic Ocean, the Bering Sea, and the Sea of Okhotsk in both DJF and JJA (Figs. 3e,f and 4e,f). The SIT change is similar to the SIC change, but it has larger values over the Arctic Ocean (Figs. 3e,f) and smaller values over the Bering Sea and the Sea of Okhotsk (not shown). The time-varying pacemaker simulations show weaker SAT and SIC responses than the idealized pacemaker simulations and produce cooling and small SIC increases over the northern Greenland, Barents, and Kara Seas and warming and SIC reduction over the Chukchi Sea in DJF (Figs. 3g,h). These temperature and sea ice changes are consistent with previous studies about the influence of PNA pattern (Liu et al. 2021) and PMV (Screen and Francis 2016; Screen and Deser 2019; X.-Y. Yang et al. 2020; Svendsen et al. 2021) on the temperature and sea ice over the Pacific sector of the Arctic.

The DJF and JJA sea ice response patterns are anticorrelated with the surface latent and sensible heat fluxes and surface upward LW radiation responses (Figs. 4e–h), with the JJA anticorrelation being stronger than the AMV case (Figs. 4a–d). The flux change is positive (i.e., upward) over the Greenland and Barents Seas in DJF (Figs. 4e,g), which is expected as sea ice acts as an insulation layer in winter. The anomalous surface upward LW radiation is strong over the Greenland and Barents Seas where sea ice decreases (Figs. 4e–h) and SAT increases (Figs. 3e–h). This suggests a positive feedback process as discussed in the AMV case (Dai et al. 2019; Dai and Jenkins 2023).

b. *The roles of atmospheric energy transport and low clouds*

One key question to consider is to what extent the impacts of AMV or PMV on Arctic SAT and SIC are due to AMV- or PMV-induced changes in atmospheric versus oceanic heat transport and convergence. Here, we first analyze the role of AMV- and PMV-induced atmospheric energy convergence, while the role of oceanic heat transport will be analyzed in the next section. We emphasize that due to the mixing of the effects from Arctic local feedbacks and remote influences on atmospheric and oceanic energy transport as discussed in section 2d, it is challenging to accurately quantify the effects of the remote influences alone, although they could be quantified using prescribed SST experiments.

During DJF, the difference in atmospheric energy transport convergence between AMV warm and cold phases is negative (i.e., it is a divergence) over the regions with negative SIC difference and the opposite is also true, such as the Davis and Denmark Straits, Labrador, Greenland, Barents, and Bering Seas and Sea of Okhotsk (Figs. 5a,c). This suggests that the sea ice loss-induced local warming leads to an atmospheric energy divergence; thus, the change in the atmospheric energy transport is largely a result, not a cause, of the local warming and sea ice loss during DJF over the MIZ. Nevertheless, Figs. 5a and 5c indicate a contribution of atmospheric energy transport from Nunavut in Canada (as illustrated by the arrows in Fig. 5a) and Greenland (Figs. 5a,c) toward the Barents Sea to the sea ice loss over the Barents Sea during DJF. Furthermore, the energy transport could lead to the warming and moistening over the Barents Sea as indicated by the increased SAT and downward LW radiation there (Figs. 3a,c and 5a,c). This warming and moistening can reduce the growth rate of sea ice over the Barents Sea, thus triggering the sea ice feedback discussed in section 3a. Less sea ice cover leads to increased surface turbulent and LW fluxes (Figs. 4a,c) into the atmosphere in winter over the Barents Sea, thereby increasing local atmospheric energy and causing large energy divergence shown in Figs. 5a and 5c over the Barents Sea. In summary, increased atmospheric energy transport toward the Barents Sea causes warming and moistening there, which triggers a local sea ice feedback in winter over the Barents Sea, thus resulting in large atmospheric warming and energy divergence there. Our results agree with a recent study by Zhang et al. (2023), who used observations and a climate model to show that a frequency increase in early winter atmospheric rivers (i.e., intense moisture transport over long and narrow regions) over the Barents–Kara Seas and the adjacent central Arctic Ocean from 1979 to 2021 contributed to 34% of the sea ice cover loss over these regions by enhancing downward LW radiation and rainfall.

In contrast to DJF, JJA sea ice loss does not enhance upward energy fluxes (Figs. 4b,d). In the idealized pacemaker runs during JJA (Fig. 5b), positive differences in atmospheric energy convergence and surface downward LW radiation and negative SIC differences are located over the Baffin Bay, Beaufort, Chukchi, Laptev, and Barents Seas. These results suggest that JJA sea ice loss does not enhance atmospheric warming, and the remotely induced atmospheric warming over those regions contributes to the summer Arctic SIC loss through increased downward LW radiation. During JJA,

←

time-varying Atlantic pacemaker simulations and CESM1-LE. Shading is shown only over the regions where the SIC differences are above the 90% confidence level based on a two-sided Student's *t* test for the idealized pacemaker ensemble and a bootstrap method with 10 000 resamples for the time-varying pacemaker ensemble. Solid (dashed) contours are for positive (negative) values, and the zero contour is omitted. The titles include the spatial pattern correlation coefficients (from left to right) between the SAT and SIC differences and between the SAT and SIT differences. (e)–(h) As in (a)–(d), but for the idealized and time-varying PMV/Pacific pacemaker ensembles.

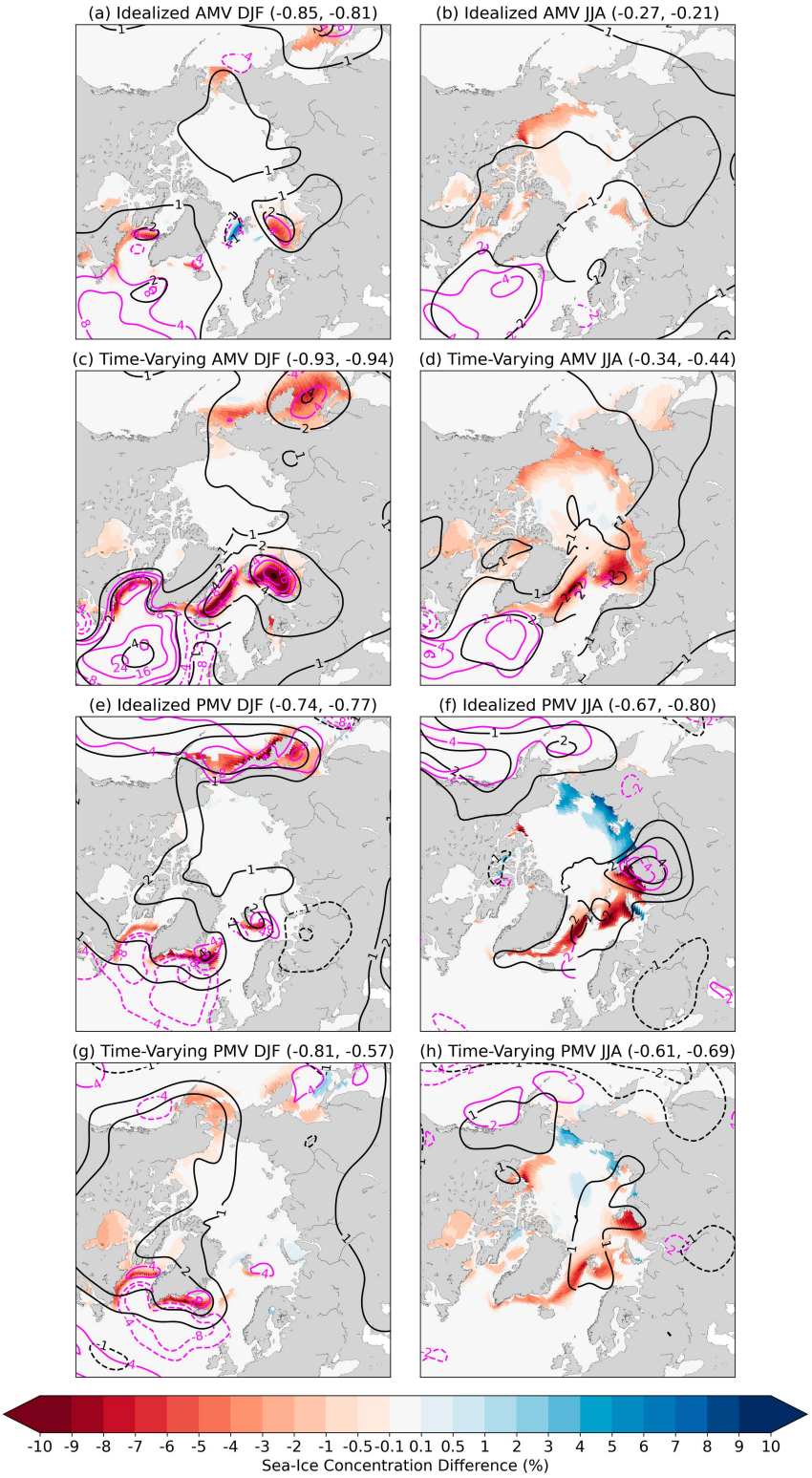

FIG. 4. As in Fig. 3, but for the SIC (%; shading), sum of surface LH and SH fluxes (W m^{-2}; positive upward; magenta contours with an interval of 2 W m^{-2} for JJA and with values of ±4, ±8, ±16, and ±24 W m^{-2} for DJF), and surface upward LW radiation (W m^{-2}; black contours with values of ±1, ±2, ±4, and ±8 W m^{-2}). The titles include the spatial pattern correlation coefficients (from left to right) between the SIC and sum of surface LH and SH fluxes differences and between the SIC and surface upward LW radiation differences.

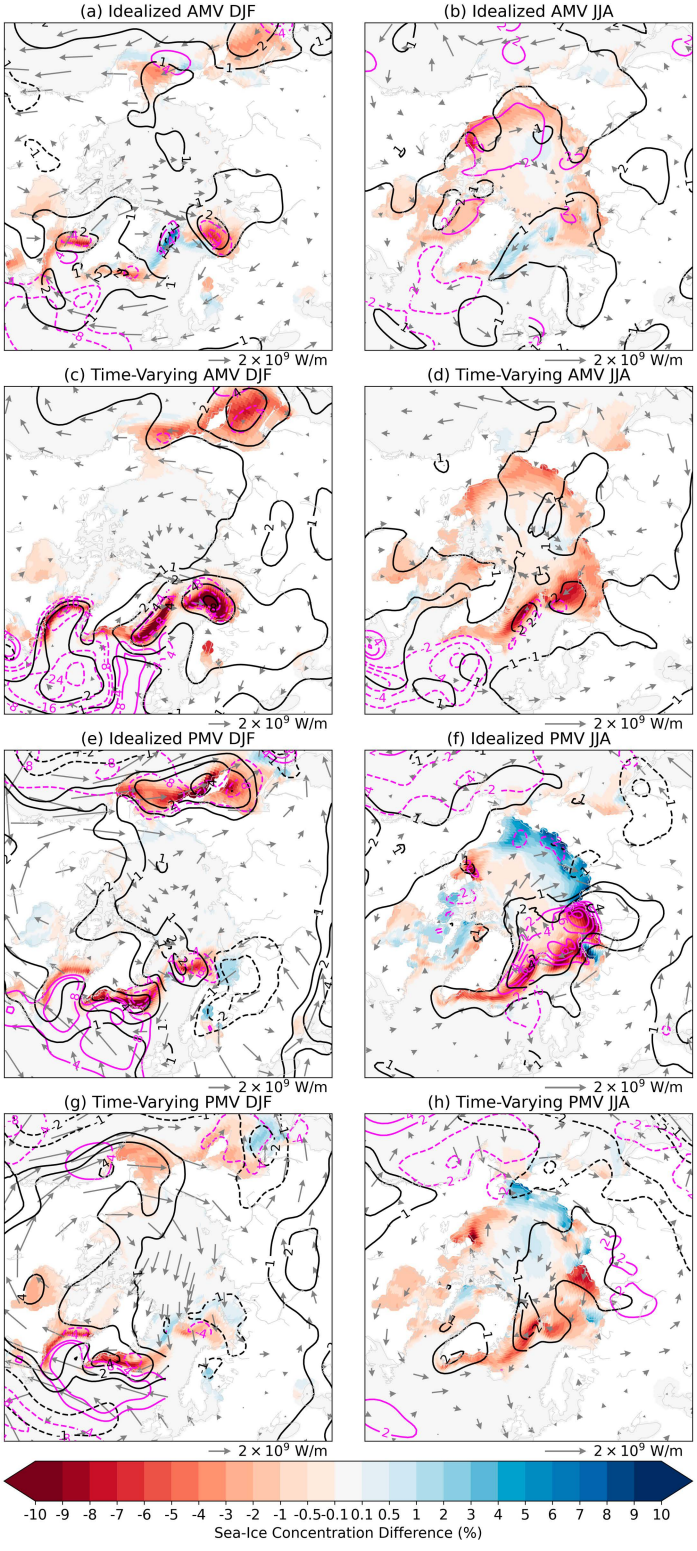

FIG. 5. Differences in the 10-yr averaged ensemble means of (a) DJF and (b) JJA SIC (%; shading), atmospheric energy transport convergence $-\nabla \cdot \mathbf{F}_A$ (W m^{-2}; magenta contours with an interval of 2 W m^{-2} for JJA and with values of ±4, ±8, ±16, and ±24 W m^{-2} for DJF), surface downward LW radiation (W m^{-2}; black contours with values of ±1, ±2, ±4, and ±8 W m^{-2}),

surface-to-air temperature differences are relatively small, leading to the low sensitivity of surface fluxes to sea ice cover (Dai et al. 2019). As a result, surface warming and surface turbulent and LW fluxes in JJA are not greatly enhanced over the MIZ, unlike in DJF (Figs. 3a–d and 4a–d). Most of the JJA Arctic warming and SIC loss are likely caused by remote influences through atmospheric energy transport from Nunavut of Canada into the central Arctic Ocean (arrows in Fig. 5b). However, the time-varying pacemaker runs show energy divergence response over the Greenland and Barents Seas and weak energy convergence response over the rest of the MIZ (Fig. 5d).

Castruccio et al. (2019) also used the idealized AMV pacemaker simulations to investigate the AMV-induced atmospheric impacts on Arctic sea ice. However, they focused on the Arctic surface energy budget and sea ice drift associated with the Arctic anticyclone/cyclone frequency. Here, we show that atmospheric energy transport and resultant Arctic warming and moistening-induced intensified downward LW radiation are important for the Arctic response to AMV-related SST forcing, especially during boreal summer, while the local sea ice feedback also plays a major role in winter.

Next, we examine whether the SAT and SIC responses are related to anomalous PMV-induced atmospheric energy transport and its convergence. During DJF, the atmospheric energy transport from northwestern North America into the Arctic (arrows in Figs. 5e,g) may warm and moisten the Arctic. The difference in atmospheric energy transport convergence between warm- and cold-phase PMV is negative in DJF over the Bering, Greenland, and Barents Seas and the Sea of Okhotsk, where negative SIC differences dominate (Figs. 5e,g). This suggests, similar to the AMV case, that the atmospheric energy convergence change occurs mainly in response to, rather than as a cause of, sea ice loss over these regions.

In JJA, there are a positive (negative) atmospheric energy convergence difference and a positive (negative) downward LW difference over the Greenland, Barents, and Kara Seas (Chukchi and East Siberian Seas) in the difference between the warm-phase and cold-phase PMV idealized pacemaker simulations (Fig. 5f), which suggest that the warm-phase PMV may influence SIC over these regions through warming and moistening (cooling and drying) of the lower troposphere (Fig. 3f) and thus increased (reduced) downward LW radiation over those regions during boreal summer. However, the time-varying pacemaker runs only show a positive downward LW response over the Greenland and Kara Seas, but do not display anomalous atmospheric energy convergence over these regions (Fig. 5h). Earlier studies by Screen and Francis (2016), X.-Y. Yang et al. (2020), Liu et al. (2021), and Svendsen et al. (2021) showed that the warm (cold) phase of PMV affects Arctic SIC by strengthening (weakening) the Aleutian low and thus changing the atmospheric heat advection over the high latitudes, as well as generating an anticyclonic (cyclonic) anomaly over the Arctic Ocean which enhances (weakens) subsidence, adiabatic warming, and hence downwelling LW radiation over the Arctic. Here, our results further show that during the warm PMV phase, the enhanced downwelling LW radiation associated with the anticyclonic anomaly over the Arctic might reduce summertime SIC on the Atlantic side.

Besides atmospheric energy transport, changes in downward LW radiation emitted by Arctic low clouds (cloud top height < 3 km) could also affect Arctic SAT and SIC. The warm-phase AMV increases low cloud cover over most of the Arctic relative to the cold-phase AMV, except over the Greenland Sea (Figs. 6a–d). Accordingly, downward LW cloud radiative forcing (which is defined as the difference between the all-sky and clear-sky net LW fluxes at the surface) is enhanced over most of the Arctic, except over the Greenland Sea and near Svalbard (Figs. 6a,b). The responses of DJF low cloud cover and downward LW cloud radiative forcing are stronger in the time-varying pacemaker runs than in the idealized pacemaker runs (Figs. 6a,c), which is consistent with the SIC response (Figs. 3a,c). The cloud LW forcing change is anticorrelated with the SIC (and to a lesser extent the SIT) change, as indicated by the negative spatial correlations between them for both DJF and JJA (Figs. 6a–d). This indicates that the increase (decrease) in low-level clouds could enhance (reduce) surface downward LW radiation and hence contribute to a decrease (increase) in sea ice, although during the summer increased clouds could also reduce downward shortwave (SW) radiation. This result is consistent with Kapsch et al. (2016), who showed that a downward LW radiation perturbation has larger impacts on summer sea ice cover than an equivalent downward SW radiation perturbation because downward LW radiation directly contributes to sea ice melting, while a large fraction of downward SW radiation is reflected by the surface. Castruccio et al. (2019) showed similar results using the idealized pacemaker simulations, but here we expand the analyses to include the time-varying pacemaker simulations. Castruccio et al. (2019) suggested that during polar winter, when solar radiation is very low, cloud LW radiative forcing becomes an important factor for the surface energy budget, and thus, Arctic surface temperature and sea ice are strongly affected by the low-level cloud cover. An

←

and vertically integrated atmospheric energy flux $\mathbf{F}_A$ (W m^{-1}; vectors) between the idealized warm- and cold-phase AMV pacemaker simulations. (c),(d) As in (a) and (b), but for the warm-phase minus cold-phase composite differences in the 11-yr moving averaged data from the ensemble mean difference between the time-varying Atlantic pacemaker simulations and CESM1-LE. Solid (dashed) contours are for positive (negative) values, and the zero contour is omitted. (e)–(h) As in (a)–(d), but for the idealized and time-varying PMV/Pacific pacemaker ensembles.

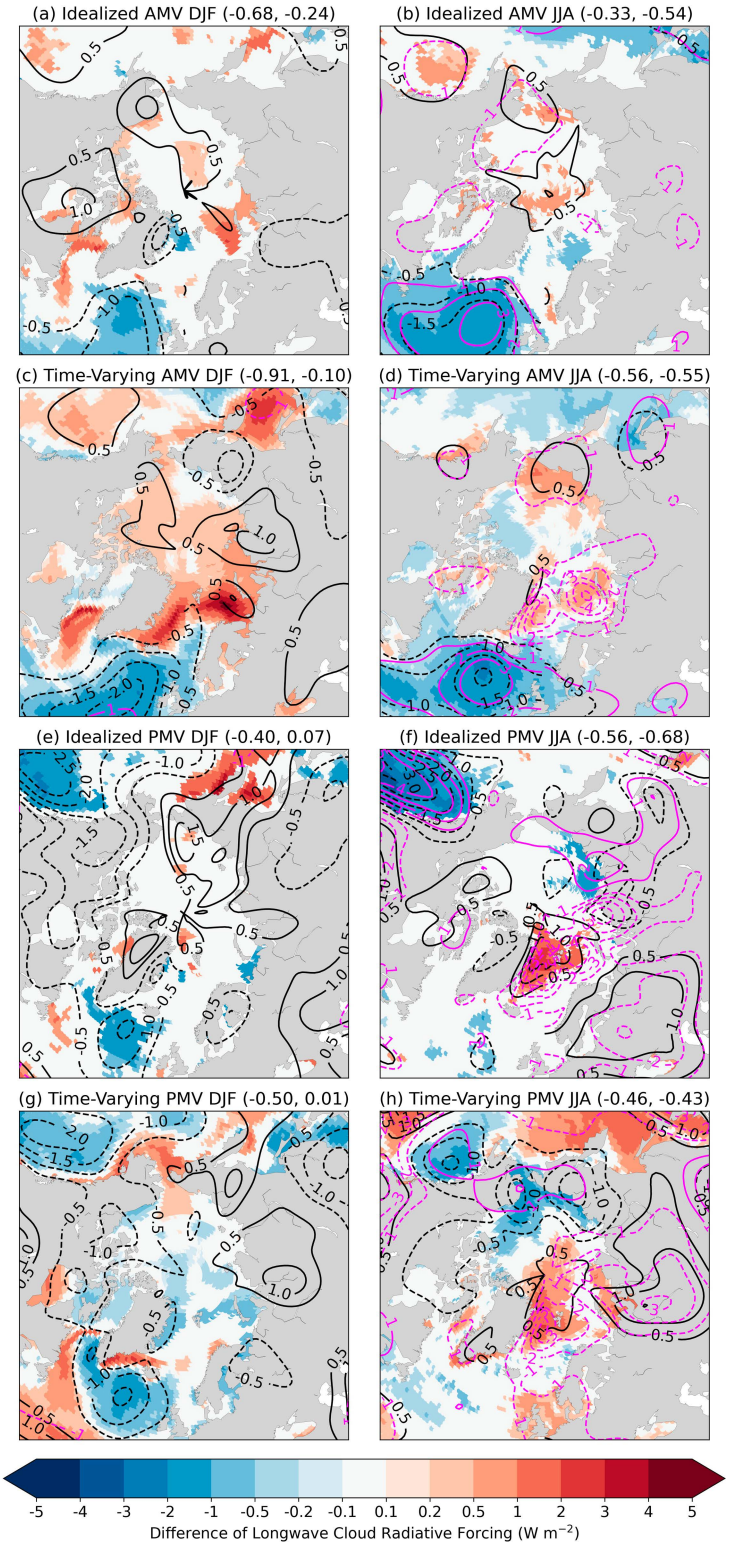

FIG. 6. As in Fig. 3, but for surface LW cloud radiative forcing (shading), surface SW cloud radiative forcing (magenta contours with an interval of 1 W m^{-2}), and low-level cloud cover (% of the sky; black contours with an interval of 0.5%). The forcing fluxes are positive downward, and solid (dashed) contours are for positive (negative) values with the zero contour being omitted. Shading is shown only over the regions where the values are statistically significant at the 90% confidence level. The titles include the spatial pattern correlation coefficients (from left to right) between the LW cloud radiative forcing and SIC differences and between the LW cloud radiative forcing and SIT differences.

increase in low-level cloud cover is a result of the decrease in polar anticyclone frequency (which is related to the decrease in SLP; Figs. 8a–d) (Wernli and Papritz 2018). Indeed, Ding et al. (2017, 2019) showed that a high-pressure anomaly in the Arctic at 200 hPa during boreal summer is associated with positive temperature, moisture, and downwelling LW radiation responses in the lower troposphere, consistent with Castruccio et al. (2019) and our results, which are mainly for winter.

During JJA, the downward SW cloud radiative forcing (i.e., the difference between the all-sky and clear-sky net SW fluxes at the surface) difference between the warm and cold AMV phases is negative (i.e., less downward solar radiation) over the Arctic, which is related to the increased low cloud cover over the Arctic which reflects more sunlight (Figs. 6b,d). This indicates that the summer cloud SW radiative forcing change counteracts the influences of cloud LW radiative forcing on SAT, SIC, and SIT. Furthermore, sea ice changes can influence low clouds by altering atmospheric conditions. Recently, Jenkins et al. (2023) pointed out that Arctic sea ice loss can lead to an increase in Arctic low cloud cover during October–March by affecting lower-tropospheric stability and humidity. Similarly, Morrison et al. (2019) found that Arctic sea ice loss does not affect clouds during summer, but increases clouds during fall.

In DJF, the warm-phase PMV is associated with positive low cloud cover and LW cloud radiative forcing responses over the Sea of Okhotsk (Figs. 6e,g), where SIC decreases (Figs. 4e,g). Moreover, the warm-phase PMV decreases JJA low cloud coverage over the East Siberian Sea (and Chukchi Sea in the time-varying pacemaker ensemble) relative to the cold-phase PMV, which reduces downward LW radiation emitted by low-level clouds over the East Siberian Sea and hence increases sea ice concentration and thickness over this region, as indicated by the negative correlation coefficients between the LW cloud radiative forcing response and SIC and SIT responses (Figs. 6f,h). Over the Greenland Sea (and Kara Sea in the time-varying pacemaker ensemble), the low-level cloud cover and LW cloud radiative forcing responses are positive during the warm-phase PMV relative to the cold-phase PMV, consistent with the observed sea ice concentration and thickness reduction over this region (Figs. 6f,h). In addition, during JJA, the response of downward SW cloud radiative forcing is positive over the East Siberian and Chukchi Seas and negative over the Greenland, Barents, and Kara Seas (Figs. 6f,h), which is anticorrelated with the response of low cloud cover since more (less) low clouds reflect more (less) SW radiation back to space. Therefore, during JJA, the response of SW cloud radiative forcing could counteract the influence of LW cloud radiative forcing on Arctic SIC and SIT. These results suggest that the warm-phase PMV influences Arctic SAT and sea ice concentration and thickness by modulating Arctic low-level cloud cover and hence LW and SW cloud radiative forcing. The changes seen in Arctic low cloud cover are related to changes observed in Arctic SLP (Figs. 8e–h; Wernli and Papritz 2018; Castruccio et al. 2019). Ding et al. (2017, 2019) proposed that the anomalous summertime anticyclonic circulation over the Arctic contributed 30%–50% to the Arctic sea ice loss since 1979 through increased downwelling LW radiation and warming and moistening of the lower troposphere. Our results support their work and further suggest that the internal atmospheric variability seen in their studies may be related to the PMV. Furthermore, the low cloud changes are not just a cause of the SIC changes, and they can also be a result of the Arctic SIC changes (Jenkins et al. 2023).

c. *The role of oceanic heat transport*

Next, we discuss whether the AMV can affect the Arctic sea ice by influencing oceanic heat convergence and transport into the Arctic. Figures 7a–d show that there is very little change in the oceanic heat flux into the Arctic region between the AMV warm and cold phases. Although the oceanic heat flux change in the subpolar North Atlantic is large, it does not reach the Arctic Ocean. Thus, the change in oceanic heat transport is not a major contributor to Arctic SAT and SIC changes, unlike atmospheric energy transport whose changes reach the central Arctic (Figs. 5a–d) and therefore can contribute to Arctic warming (Figs. 3a–d). During DJF, the estimated differences in oceanic heat transport convergence between AMV warm and cold phases are positive over the regions with negative SIC difference and the opposite is also true, such as the Davis and Denmark Straits, Labrador, Greenland, Barents, and Bering Seas and the Sea of Okhotsk (Figs. 7a,c). Further examination of the F_{net} and $\partial O_E/\partial t$ terms in Eq. (5) reveals that the net surface heat flux term F_{net} dominates over regions with large sea ice loss, where F_{net} is strongly negative in DJF (i.e., upward; Figs. A3a,c and A4a,c). This is consistent with the increased upward surface heat and LW fluxes over the MIZ with large sea ice loss (Figs. 4a,c). The relatively small tendency of mixed layer ocean heat content $\partial O_E/\partial t$ implies that the increased upward surface net heat flux F_{net} comes mainly from increased horizontal (i.e., $-\nabla \cdot \mathbf{F}_O$) and/or vertical (i.e., F_D) heat convergence in the ocean mixed layer, rather than from local energy storage changes. This local heat convergence might be initiated by the local oceanic cooling (and the resultant horizontal and vertical oceanic temperature gradient) to supply the necessary energy for the increased heat release to the air (i.e., F_{net}) due to sea ice loss. The buoyancy loss from the mixed layer associated with upward F_{net} could drive vertical mixing with deeper waters, in which case there might be an approximate balance $F_{\text{net}} \approx -F_D$. In this way, oceanic heat convergence, surface heat flux, and SIC are coupled with each other, and it is challenging to discuss their causality using our method. However, other studies (e.g., Dai et al. 2019; Dai and Jenkins 2023) suggest that the SIC change is the main driving factor for winter Arctic surface flux changes, which is consistent with the small changes in the oceanic heat flux over the Arctic Ocean (Figs. 7a–d), thus suggesting that Arctic sea ice variability could also influence the AMV (Liu et al. 2019; Deng and Dai 2022).

During JJA, the SIC changes are positively correlated with the estimated oceanic heat convergence response over the Greenland, Barents, East Siberian, Chukchi, and Beaufort Seas (i.e., the sea ice loss is associated with oceanic heat

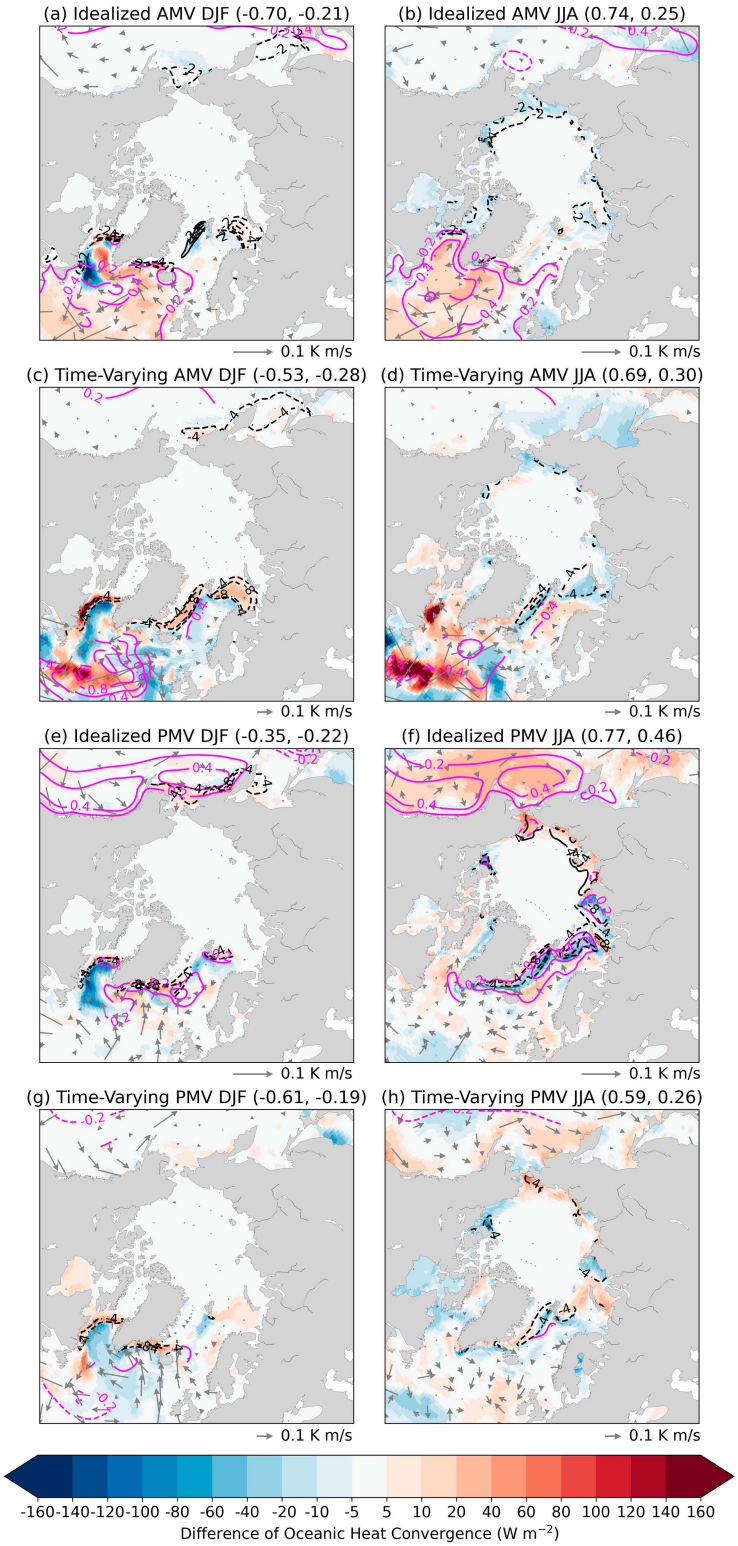

FIG. 7. As in Fig. 5, but for differences in oceanic heat transport convergence $-\nabla \cdot \mathbf{F}_O + F_D$ (W m^{-2}; shading; the values for JJA are multiplied by a factor of 5 for visualization), SST (°C; magenta contours with an interval of 0.2°C), SIC [%; black contours with an interval of 2% for (a) and (b), and with values of ±4%, ±8% for (c)–(h)], and 5-m oceanic heat flux (K m s^{-1}; vectors). The titles include the spatial pattern correlation coefficients (from left to right) between the oceanic heat transport convergence and SIC differences and between the oceanic heat transport convergence and SIT differences.

divergence; Figs. 7b,d). This is consistent with the fact that during summer, the ocean absorbs more solar radiation over areas with less sea ice cover, which increases local ocean temperature and thus leads to heat divergence. Thus, in this case, the estimated oceanic heat divergence change is also a result of the F_{net} change caused by sea ice loss.

In summary, the AMV-related SST forcing does not cause significant changes in oceanic heat fluxes over the Arctic Ocean; thus, oceanic heat transport contributes little to Arctic SAT and SIC changes. The local changes in oceanic heat flux convergence over the MIZ are likely caused by SIC-induced surface flux changes, rather than a cause of the SIC change, for both DJF and JJA.

Next, we discuss whether the PMV-related oceanic circulation contributes to Arctic sea ice variability. In the idealized and time-varying pacemaker runs, during the PMV warm phase in DJF, increased oceanic heat transport convergence is collocated with the SIC decrease over the Denmark Strait, Labrador, Greenland, Barents, and Bering Seas, when compared to the PMV cold phase (Figs. 7e,g). The response of the net surface heat flux F_{net} is dominant over regions of large SIC variations (Figs. A3e,g and A4e,g), which suggests that the SIC variations affect surface heat fluxes between the ocean and the atmosphere, hence changing ocean temperature and its gradients in both horizontal and vertical directions, driving anomalous horizontal and vertical oceanic heat fluxes, and leading to the oceanic heat convergence or divergence. On the other hand, changes in upper ocean temperatures caused by oceanic heat transport or surface fluxes can also affect SIC, making it difficult to disentangle their relationships (Dai and Jenkins 2023). During JJA, the estimated oceanic heat convergence response is negative (positive) in the regions of SIC decrease (increase) (Figs. 7f,h). Such regions include all the Seas in the peripheral Arctic Ocean. This result indicates that the oceanic heat convergence change is an effect of the change in absorption of solar radiation, rather than a cause of sea ice variations.

d. The roles of dynamic and thermodynamic processes

Next, we discuss whether the AMV-induced surface wind anomalies can also influence Arctic sea ice through changes in sea ice motion. Figure 8a shows that in the idealized AMV pacemaker ensembles, warm-phase AMV enhances transpolar sea ice drift over the central Arctic Ocean with anomalous southward sea ice motion near Svalbard in DJF, consistent with the SIC increase over the Greenland and western Barents Seas, as SIC is larger at higher latitudes. During DJF, the sea ice motion response is convergent (divergent) and the SLP response is positive (negative) over the Greenland Sea in the idealized (time varying) pacemaker runs, which is related to the SIC increase (decrease) in this region (Figs. 8a,c). During JJA, the response of sea ice drift is weaker than during DJF, and the flow toward lower latitudes is choked at the Fram Strait and the western Barents Sea (Fig. 8b). The time-varying Atlantic pacemaker ensemble shows similar results as the idealized pacemaker ensemble except over the Greenland Sea (Figs. 8c,d). The warm-phase AMV induces a La Niña–like SSTA pattern over the Pacific (Figs. A1a,c) and hence weakens the Aleutian low (Figs. 8a,c) and generates anomalous southwesterly winds over the Bering Sea (not shown), which results in anomalous sea ice movement toward the northeast that may decrease Bering Sea's SIC (Figs. 8a–d). This result was also shown by Castruccio et al. (2019) using idealized AMV pacemaker runs. Moreover, the atmosphere–ocean–ice feedbacks discussed in sections 3a–3c can amplify the SIC response caused by anomalous sea ice motion.

Furthermore, we compare the SIC tendencies due to dynamical and thermodynamical processes in the AMV/Atlantic pacemaker simulations. The SIC tendency due to dynamic processes is largely caused by horizontal transport and mechanical deformation associated with horizontal winds and ocean currents. The SIC tendency due to thermodynamics is caused by freezing and melting at the ice–atmosphere interface and ice–ocean interface, as well as lateral growth. During DJF, the dynamical and thermodynamical contributions to Arctic SIC tendencies have similar magnitudes over most of the Arctic Ocean (Figs. 9a,c). During JJA, the SIC tendencies due to dynamics are weaker than the SIC tendencies due to thermodynamics over most of the Arctic, except over some regions in the central Arctic Ocean (Figs. 9b,d). These results suggest that the dynamic processes are as important as the local thermodynamic processes for the impacts of AMV on winter Arctic SIC, but they are less important in JJA over the MIZ and more important over the central Arctic Ocean.

In addition, the PMV can influence Arctic sea ice concentration and thickness by generating anomalous sea ice drift. During JJA, there is an anticyclonic sea ice drift difference over the East Siberian and Laptev Seas between the PMV's warm phase and cold phase (Figs. 8f,h). The anomalous sea ice drift from the North Pole toward the northern Russian coast is observed over the East Siberian and Laptev Seas, and the opposite is true over the Barents and Kara Seas (Figs. 8f,h), consistent with the anomalous SLP, 850-hPa winds (not shown), and the SIC responses over these regions (because Arctic SIC is higher in regions closer to the North Pole). Moreover, during the PMV warm phase in DJF, anomalous sea ice motion divergence (relative to the PMV cold phase) is observed in the Bering Sea, consistent with the SIC decrease over this region. Furthermore, anomalous northeastward sea ice drift occurs over the Denmark Strait, which might reduce SIC locally (Figs. 8e–h).

The dynamic and thermodynamic contributions of PMV to the Arctic SIC variations have similar intensities during DJF (Figs. 9e,g). During JJA, the SIC tendencies due to dynamics are weaker than the SIC tendencies due to thermodynamics over most of the Arctic Ocean except the central Arctic Ocean on the North American side (Figs. 9f,h). Hence, during DJF, the dynamic processes are equally important as the thermodynamic processes for the PMV impacts on Arctic SIC, while during JJA, they are less (more) important over most of the MIZ (central Arctic Ocean). This result is similar to the result for AMV.

4. Summary and discussion

Previous work (e.g., Chylek et al. 2009, 2010; Mahajan et al. 2011; Day et al. 2012; Zhang 2015; Castruccio et al. 2019;

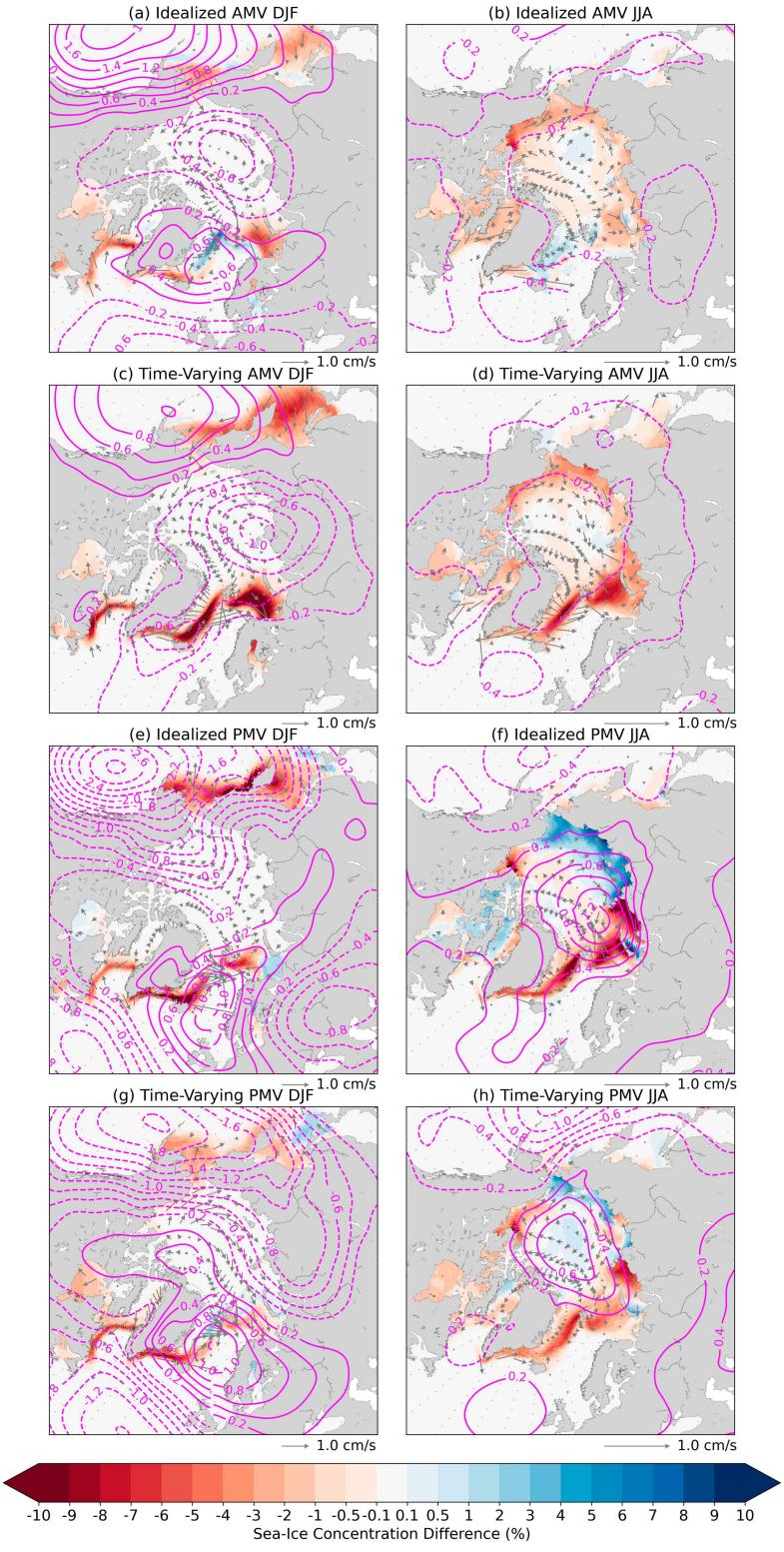

FIG. 8. Differences in 10-yr averaged ensemble means of (a) DJF and (b) JJA sea ice velocity (cm s^{-1}; vectors), SIC (%; shading), and SLP (hPa; magenta contours with an interval of 0.2 hPa) between the idealized warm- and cold-phase AMV pacemaker simulations. (c),(d) As in (a) and (b), but for the warm-phase minus cold-phase composite differences in the 11-yr moving averaged data from the ensemble mean difference

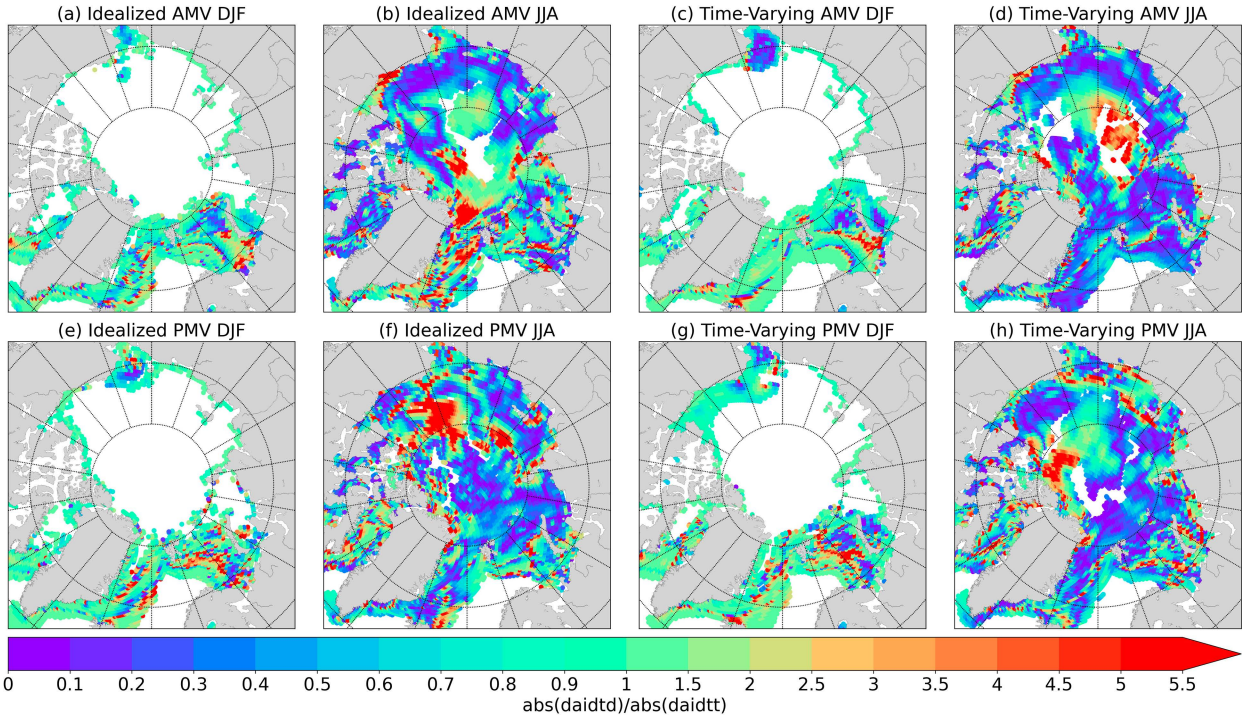

FIG. 9. The ratios of the absolute values of 10-yr averaged ensemble mean differences in (a) DJF and (b) JJA SIC tendency due to dynamical processes and SIC tendency due to thermodynamic processes between the idealized warm- and cold-phase AMV pacemaker simulations. (c),(d) As in (a) and (b), but for the warm-phase minus cold-phase composite differences in the 11-yr moving averaged data from the ensemble mean difference between the time-varying Atlantic pacemaker simulations and CESM1-LE. (e)–(h) As in (a)–(d), but for the data from the idealized PMV and the time-varying Pacific pacemaker runs. The values are shown only over regions where the SIC response is stronger than 0.05%.

Screen and Deser 2019; X.-Y. Yang et al. 2020; Liu et al. 2021; Svendsen et al. 2021) has estimated the contribution of AMV and PMV to Arctic sea ice loss rate and discussed the processes involved in the influences of AMV and PMV on Arctic sea ice. However, these studies have not quantified these influences and related processes. In this study, we analyzed the idealized and time-varying AMV/Atlantic and PMV/Pacific pacemaker simulations performed at NCAR using CESM1 to investigate to what extent the internal components of AMV and PMV can influence Arctic sea ice concentration (SIC) and sea ice thickness (SIT), explore the relative roles of associated processes, and compare our results with previous studies. The results suggest that up to 0.25×10^{12} m^2 (2.7% of the 1920–2013 mean) of the sea ice area and 0.24×10^{13} m^3 (8.3%) of the sea ice volume variations may be attributed to the AMV and up to 0.14×10^{12} m^2 (1.4% of the 1920–2013 mean) of the sea ice area and 0.20×10^{13} m^3 (7.0%) of the sea ice volume variations may be due to the PMV during 1920–2013. The SIT variations occur over the whole Arctic Ocean, while the SIC variations occur mainly over the marginal ice zone. In addition, we showed that both the AMV and PMV can accelerate or slow down the forced SIC trend by more than 50% on decadal time scales over the MIZ during their warm or cold phases and their phase shift periods.

Our results show that the SIC and SIT decrease over most of the Arctic in response to the warm-phase AMV is related to widespread warming in the lower troposphere over the Arctic, due to increased poleward energy transport in the atmosphere and enhanced surface downward LW radiation. Analysis of time-varying Atlantic pacemaker simulations also indicates that Arctic SIC is influenced by anomalous sea ice motion, low cloud cover, and its downward LW radiative forcing, which are related to changes in SLP and the polar anticyclone frequency, as discussed in an earlier study based on idealized Atlantic pacemaker runs (Castruccio et al. 2019). Our findings extend those of Castruccio et al. (2019), confirming the effects of atmospheric teleconnections from AMV on Arctic sea ice and suggesting that poleward heat and moisture

←
between the time-varying Atlantic pacemaker simulations and CESM1-LE. Solid contours are for positive values, dashed contours are for negative values, and the zero-contour line is omitted. (e)–(h) As in (a)–(d), but for the idealized and time-varying PMV/Pacific pacemaker ensembles.

transport (thermodynamic effect) and sea ice motion (dynamic effect) serve as triggers of sea ice changes. Previous studies (e.g., Mahajan et al. 2011; Zhang 2015) show that the AMV affects Arctic sea ice through changing oceanic heat transport. However, we found little change in oceanic heat transport into the Arctic in response to AMV. Moreover, we show that winter oceanic heat convergence/divergence in the MIZ is mainly a result of the SIC reduction/increase caused by AMV-induced Arctic warming/cooling that is amplified by the positive local atmosphere–ocean–ice feedback (Dai and Jenkins 2023). We also quantify the relative importance of thermodynamical and dynamical processes for the SIC response to AMV. Changes in sea ice motion and thermodynamic changes overall contribute similarly to the AMV-induced DJF SIC variability, while in JJA the sea ice motion contribution is lower than the thermodynamic factor over the MIZ but higher over parts of the central Arctic.

Furthermore, our results suggest that, in winter, the reduction in sea ice enhances upward energy fluxes, which heat near-surface air and warm the lower troposphere. This lower-tropospheric warming in turn leads to increased downward LW radiation and further sea ice reduction, resulting in positive feedback, as shown previously (Dai et al. 2019; Deng and Dai 2022; Dai and Jenkins 2023). This feedback could amplify and sustain the AMV-induced sea ice changes. In addition, the pacemaker simulations capture the weakening of the Aleutian low during the warm AMV phase in winter, which relates to the anomalous sea ice motion over the Bering Sea and Sea of Okhotsk and positive SSTA over the central North Pacific. Thus, the Atlantic pacemaker runs contain not only the influence of Atlantic SSTA but also the impacts of Atlantic-induced Pacific SSTA on Arctic climate. This indicates that interbasin teleconnections need to be considered as a critical component of the influences of AMV or PMV.

During PMV warm phases, SIC and SIT increase over the Chukchi, East Siberian, and Laptev Seas and northern Canada, but decrease over other parts of the Arctic. Earlier studies (e.g., X.-Y. Yang et al. 2020; Liu et al. 2021; Svendsen et al. 2021) show that the PMV-induced SLP anomalies over the central Arctic and Bering Sea are related to sea ice changes through anomalous atmospheric heat and moisture transport, adiabatic descent and warming, downward LW radiation, and Ekman pumping. These mechanisms are consistent with our results. We further suggest that the anomalous sea ice velocity associated with the PMV-induced SLP pattern also contributes to Arctic sea ice change over the Seas near the northern Russian coast. In addition, our results extend earlier studies, suggesting that the PMV-induced atmospheric energy transport and its convergence and downward LW radiation emitted from low clouds contribute to Arctic SIC and SIT variations. As in the AMV case, the sea ice drift is as important as thermodynamic processes for the PMV-induced DJF Arctic SIC variations, but weaker than the thermodynamic processes during JJA over the MIZ and stronger than the thermodynamic processes over parts of the central Arctic Ocean. Our results also show that the sea ice decrease can be amplified through the atmosphere–ocean–ice feedback mentioned above. Furthermore, earlier studies (Woodgate et al. 2010; Zhang 2015) show that the anomalous northward oceanic heat transport from the Pacific to the Arctic through the Bering Strait contributed to Arctic sea ice changes. However, we suggest that oceanic heat convergence or divergence is mainly a response to the PMV-induced Arctic SIC variability over the MIZ.

In summary, our study, for the first time, quantitatively estimates the contributions of the internal components of AMV and PMV to Arctic sea ice area and volume variations using pacemaker simulations. We emphasize that the AMV- or PMV-induced anomalous atmospheric circulation affects the Arctic sea ice through poleward atmospheric energy transport, LW radiation (partly influenced by clouds), and sea ice motion. Additionally, we found that sea ice loss enhances ocean-to-air energy fluxes, which cause local ocean heat convergence and warm the lower troposphere. The latter further increases sea ice loss through downward longwave radiation. Our results suggest that atmospheric processes trigger Arctic sea ice variations, while atmosphere–ocean–ice feedbacks amplify and sustain such variations; oceanic processes are mainly responses to sea ice variations. However, some limitations are worth noting. Due to the signal-to-noise paradox, the quantitative estimates of the influences of internal AMV and PMV on Arctic sea ice area and volume shown in Figs. 1b and 1c, as well as the modeled responses of the other fields to internal AMV and PMV based on composite analysis, might be lower than the realistic values. Future work could evaluate the impacts of the externally forced (e.g., by aerosol forcing) component of AMV or PMV on Arctic sea ice by scaling the contributions of the internal component of AMV or PMV estimated in this study by the ratios of the external and internal components of the AMV or PMV index, assuming the SSTA patterns are similar for the two components. Moreover, according to Lin et al. (2019), the transport of warm and saline Atlantic water into Greenland–Iceland–Norwegian Seas is associated with the 50–80-yr AMV, but not with the 10–30-yr AMV. Future work could evaluate whether oceanic heat transport plays a substantial role in the influence of the 50–80-yr AMV on Arctic sea ice. Finally, the influences of PMV on Arctic climate could also be investigated using the CESM2-LE and the CESM2 Pacific pacemaker ensemble.

Acknowledgments. This study was supported by NSF (OISE-1743738 and DEB-1923957). A. Dai also acknowledges the support of NSF Grant AGS-2015780. The authors deeply appreciate the CESM Climate Variability & Change Working Group (CVCWG), Met Office Hadley Centre, and the National Oceanic and Atmospheric Administration (NOAA) National Centers for Environmental Information (NCEI) for providing the data used in this study. We are also grateful for insightful and constructive comments from three reviewers that helped to significantly improve the quality of this manuscript.

Data availability statement. All data used in this study are openly available online. The data of pacemaker simulations are available from the NCAR Climate Data Gateway.

Specifically, the idealized AMV pacemaker simulations are available at https://doi.org/10.26024/rn3t-ep30; the idealized PMV pacemaker simulations are available at https://www.earthsystemgrid.org/dataset/ucar.cgd.ccsm4.IPO-PACEMAKER.html; the time-varying Atlantic pacemaker simulations are available at https://www.earthsystemgrid.org/dataset/ucar.cgd.ccsm4.ATL-PACEMAKER.html; and the time-varying Pacific pacemaker simulations are available at https://www.earthsystemgrid.org/dataset/ucar.cgd.ccsm4.pac-pacemaker.html. The SST data from ERSST.v3b are available from the NOAA NCEI at https://doi.org/10.7289/V5Z31WJ4. The SIC data from HadISST1 are available from the Met Office Hadley Centre at https://www.metoffice.gov.uk/hadobs/hadisst/data/download.html.

APPENDIX

Supporting Figures

Figure A1 shows the patterns of the global SST differences between the warm-phase AMV and cold-phase AMV and between the warm-phase PMV and cold-phase PMV from the pacemaker simulations. Figure A2 compares the climatologies of Arctic SIC from the HadISST1 and CESM1-LE. Figure A3 displays the patterns of the differences in Arctic net surface heat flux between the warm-phase AMV and cold-phase AMV and between the warm-phase PMV and cold-phase PMV from the pacemaker simulations. Figure A4 displays the patterns of the differences in Arctic tendency of mixed-layer ocean heat content between the warm-phase AMV and cold-phase AMV and between the warm-phase PMV and cold-phase PMV from the pacemaker simulations.

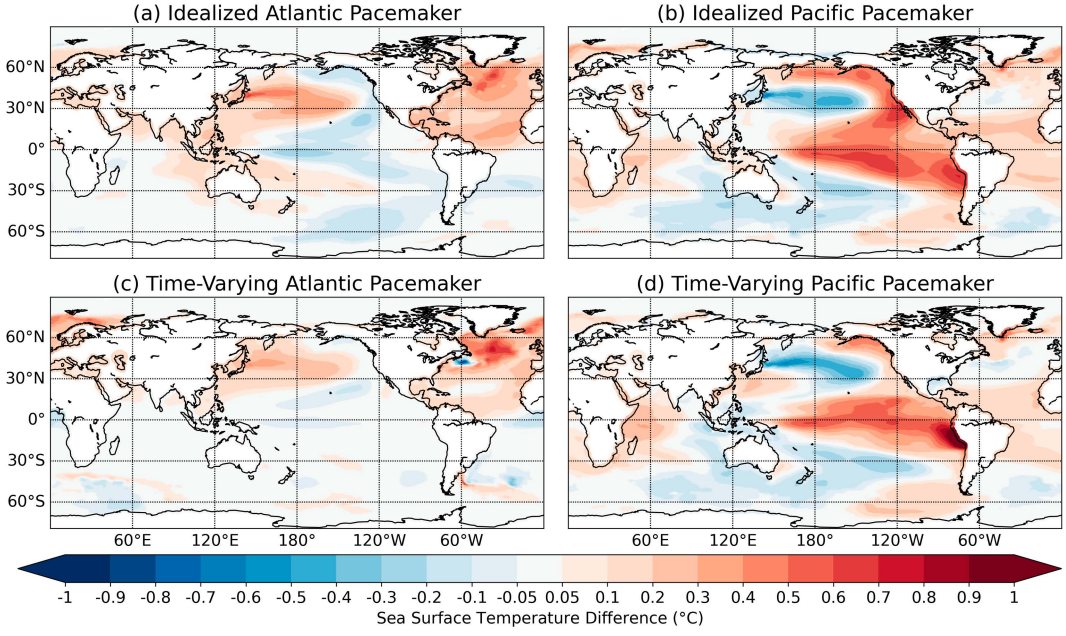

FIG. A1. Differences in the 10-yr averaged ensemble means of annual SST between (a) the warm-phase AMV and cold-phase AMV idealized pacemaker simulations and between (b) the warm-phase PMV and cold-phase PMV idealized pacemaker simulations. (c),(d) As in (a) and (b), but for the warm-phase minus cold-phase composite differences in the 11-yr moving averaged data from the ensemble mean difference between the time-varying Atlantic or Pacific pacemaker simulations, respectively, and CESM1-LE.

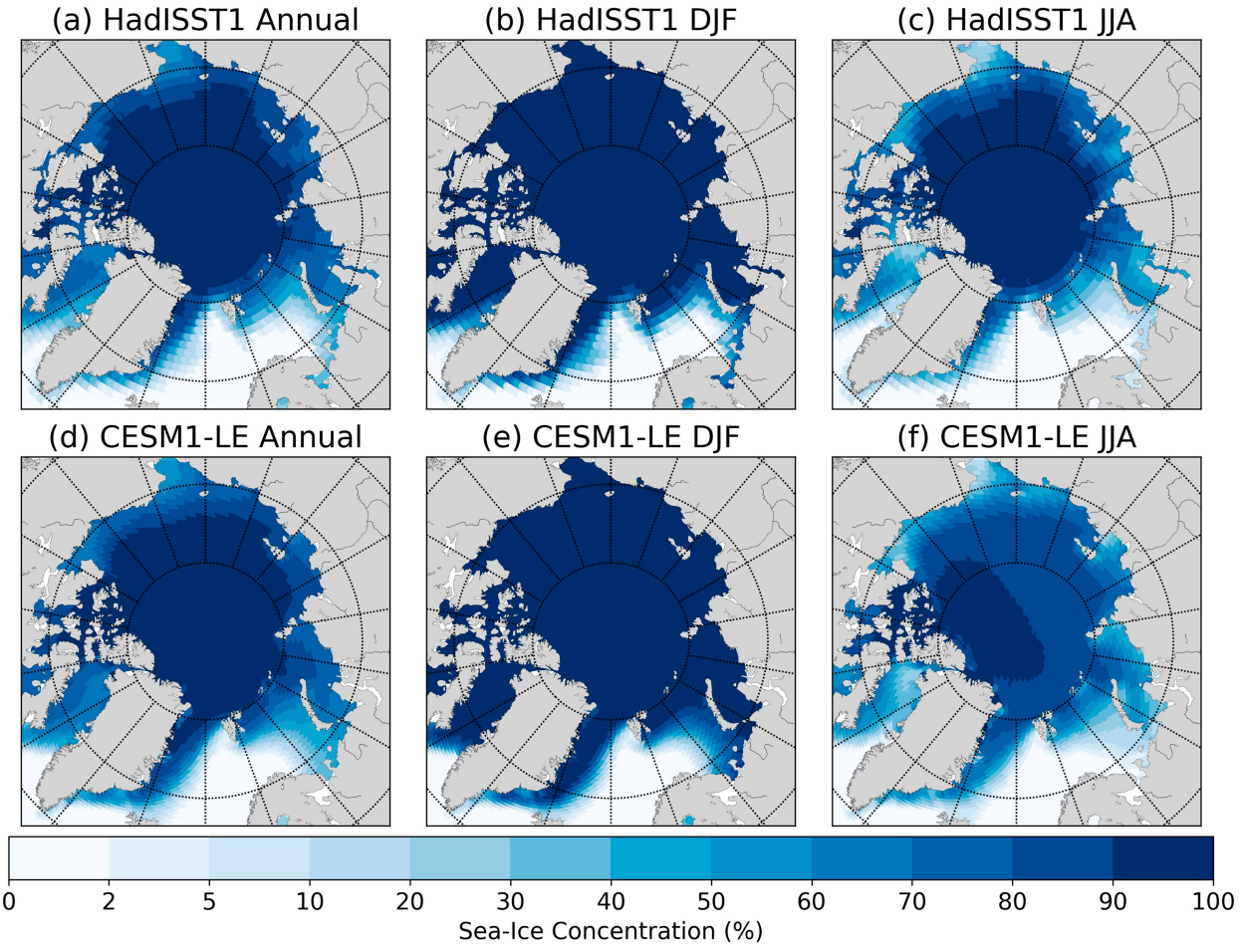

FIG. A2. SIC climatology during 1920–2013 from the (top) HadISST1 and (bottom) CESM1-LE for (a),(d) annual, (b),(e) DJF, and (c),(f) JJA.

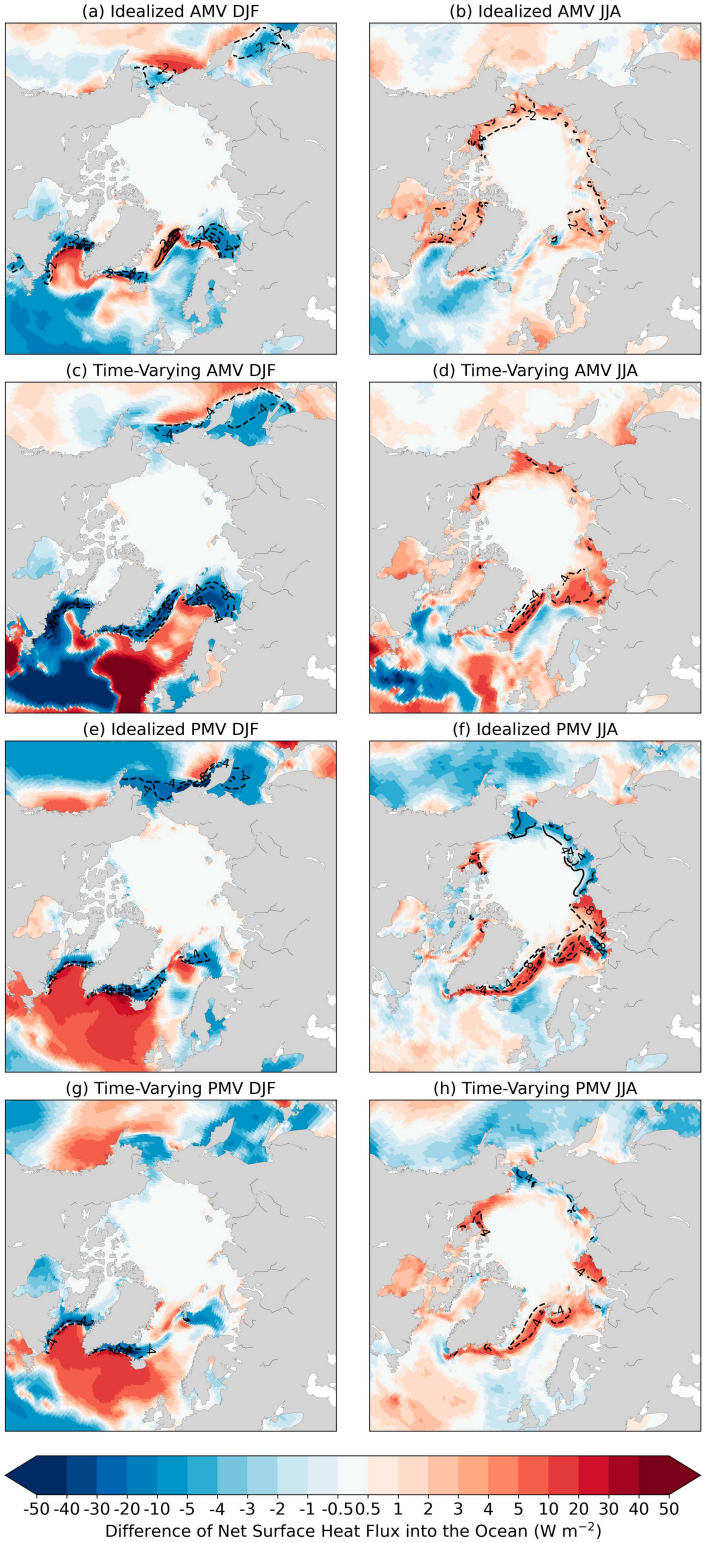

FIG. A3. Differences in the 10-yr averaged ensemble means of (a) DJF and (b) JJA net surface heat flux F_{net} (W m^{-2}; shading; positive downward) and SIC [%; black contours with an interval of 2% for (a) and (b) and with values of ±4%, ±8% for (c)–(h)] between the idealized warm- and cold-phase AMV pacemaker simulations. (c),(d) As in (a) and (b), but for the warm-phase minus cold-phase composite differences in the 11-yr moving averaged data from the ensemble mean difference between the time-varying Atlantic pacemaker

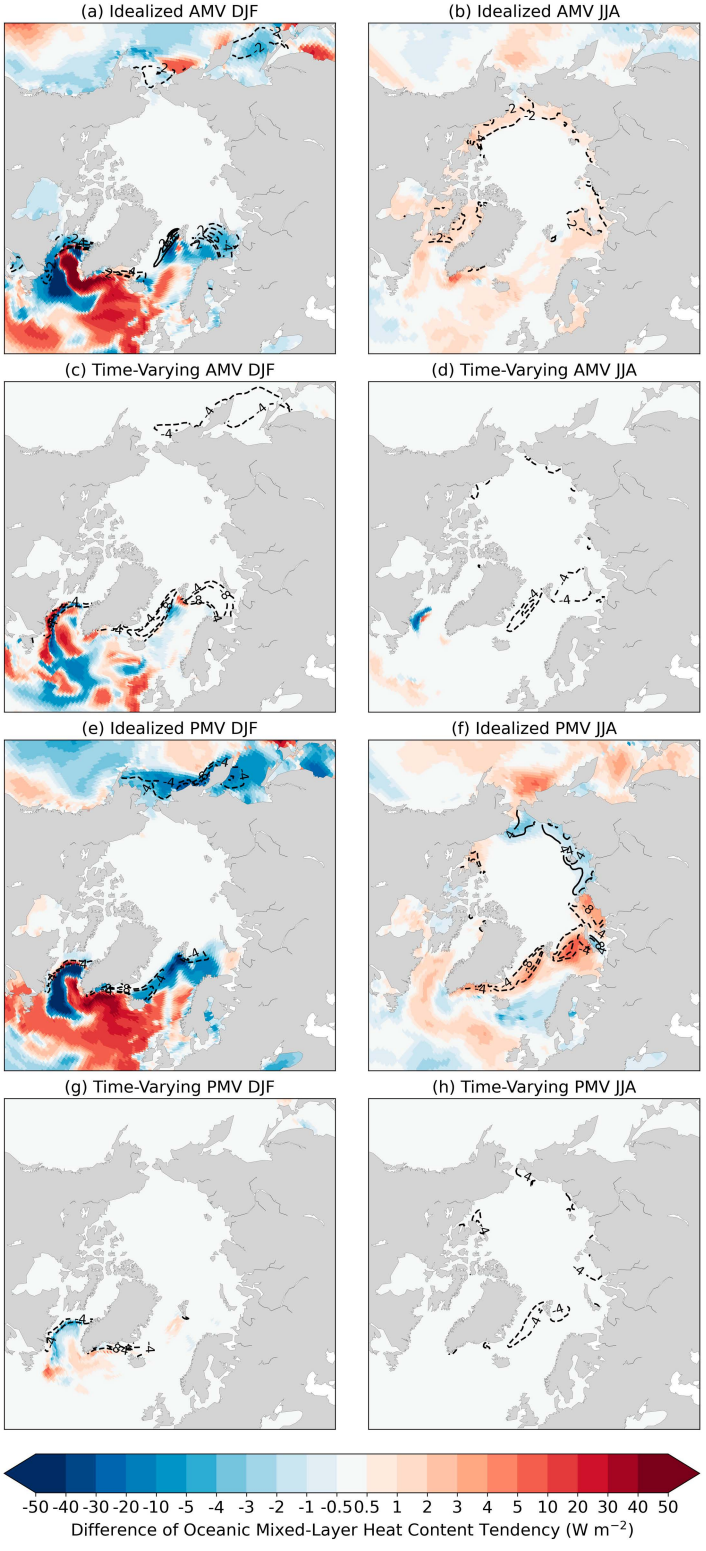

FIG. A4. As in Fig. A3, but for the tendency of mixed layer ocean heat content $\partial O_E/\partial t$.

←

simulations and CESM1-LE. Solid contours are for positive values, dashed contours are for negative values, and the zero-contour line is omitted. (e)–(h) As in (a)–(d), but for the idealized and time-varying PMV/Pacific pacemaker ensembles.

REFERENCES

Bitz, C. M., K. M. Shell, P. R. Gent, D. A. Bailey, G. Danabasoglu, K. C. Armour, M. M. Holland, and J. T. Kiehl, 2012: Climate sensitivity of the Community Climate System Model, version 4. *J. Climate*, **25**, 3053–3070, https://doi.org/10.1175/JCLI-D-11-00290.1.

Boé, J., A. Hall, and X. Qu, 2009: September sea-ice cover in the Arctic Ocean projected to vanish by 2100. *Nat. Geosci.*, **2**, 341–343, https://doi.org/10.1038/ngeo467.

Bonan, D. B., T. Schneider, I. Eisenman, and R. C. J. Wills, 2021: Constraining the date of a seasonally ice-free Arctic using a simple model. *Geophys. Res. Lett.*, **48**, e2021GL094309, https://doi.org/10.1029/2021GL094309.

Brennan, M. K., G. J. Hakim, and E. Blanchard-Wrigglesworth, 2020: Arctic sea-ice variability during the instrumental era. *Geophys. Res. Lett.*, **47**, e2019GL086843, https://doi.org/10.1029/2019GL086843.

Cai, Q., J. Wang, D. Beletsky, J. Overland, M. Ikeda, and L. Wan, 2021: Accelerated decline of summer Arctic sea ice during 1850–2017 and the amplified Arctic warming during the recent decades. *Environ. Res. Lett.*, **16**, 034015, https://doi.org/10.1088/1748-9326/abdb5f.

Castruccio, F. S., Y. Ruprich-Robert, S. G. Yeager, G. Danabasoglu, R. Msadek, and T. L. Delworth, 2019: Modulation of Arctic sea ice loss by atmospheric teleconnections from Atlantic multidecadal variability. *J. Climate*, **32**, 1419–1441, https://doi.org/10.1175/JCLI-D-18-0307.1.

Chylek, P., C. K. Folland, G. Lesins, M. K. Dubey, and M. Wang, 2009: Arctic air temperature change amplification and the Atlantic multidecadal oscillation. *Geophys. Res. Lett.*, **36**, L14801, https://doi.org/10.1029/2009GL038777.

——, ——, ——, and ——, 2010: Twentieth century bipolar seesaw of the Arctic and Antarctic surface air temperatures. *Geophys. Res. Lett.*, **37**, L08703, https://doi.org/10.1029/2010GL042793.

Comiso, J. C., C. L. Parkinson, R. Gersten, and L. Stock, 2008: Accelerated decline in the Arctic sea ice cover. *Geophys. Res. Lett.*, **35**, L01703, https://doi.org/10.1029/2007GL031972.

Dai, A., and M. T. Jenkins, 2023: Relationships among Arctic warming, sea-ice loss, stability, lapse rate feedback, and Arctic amplification. *Climate Dyn.*, **61**, 5217–5232, https://doi.org/10.1007/s00382-023-06848-x.

——, J. C. Fyfe, S.-P. Xie, and X. Dai, 2015: Decadal modulation of global surface temperature by internal climate variability. *Nat. Climate Change*, **5**, 555–559, https://doi.org/10.1038/nclimate2605.

——, D. Luo, M. Song, and J. Liu, 2019: Arctic amplification is caused by sea-ice loss under increasing CO_2. *Nat. Commun.*, **10**, 121, https://doi.org/10.1038/s41467-018-07954-9.

Day, J. J., J. C. Hargreaves, J. D. Annan, and A. Abe-Ouchi, 2012: Sources of multi-decadal variability in Arctic sea ice extent. *Environ. Res. Lett.*, **7**, 034011, https://doi.org/10.1088/1748-9326/7/3/034011.

Deng, J., and A. Dai, 2022: Sea ice–air interactions amplify multidecadal variability in the North Atlantic and Arctic region. *Nat. Commun.*, **13**, 2100, https://doi.org/10.1038/s41467-022-29810-7.

Deser, C., R. Guo, and F. Lehner, 2017: The relative contributions of tropical Pacific sea surface temperatures and atmospheric internal variability to the recent global warming hiatus. *Geophys. Res. Lett.*, **44**, 7945–7954, https://doi.org/10.1002/2017GL074273.

Ding, Q., and Coauthors, 2017: Influence of high-latitude atmospheric circulation changes on summertime Arctic sea ice. *Nat. Climate Change*, **7**, 289–295, https://doi.org/10.1038/nclimate3241.

——, and Coauthors, 2019: Fingerprints of internal drivers of Arctic sea ice loss in observations and model simulations. *Nat. Geosci.*, **12**, 28–33, https://doi.org/10.1038/s41561-018-0256-8.

Dong, B., A. Dai, M. Vuille, and O. Elison Timm, 2018: Asymmetric modulation of ENSO teleconnections by the interdecadal Pacific oscillation. *J. Climate*, **31**, 7337–7361, https://doi.org/10.1175/JCLI-D-17-0663.1.

Döscher, R., T. Vihma, and E. Maksimovich, 2014: Recent advances in understanding the Arctic climate system state and change from a sea ice perspective: A review. *Atmos. Chem. Phys.*, **14**, 13 571–13 600, https://doi.org/10.5194/acp-14-13571-2014.

England, M., A. Jahn, and L. Polvani, 2019: Nonuniform contribution of internal variability to recent Arctic sea ice loss. *J. Climate*, **32**, 4039–4053, https://doi.org/10.1175/JCLI-D-18-0864.1.

Fasullo, J. T., and K. E. Trenberth, 2008a: The annual cycle of the energy budget. Part I: Global mean and land–ocean exchanges. *J. Climate*, **21**, 2297–2312, https://doi.org/10.1175/2007JCLI1935.1.

——, and ——, 2008b: The annual cycle of the energy budget. Part II: Meridional structures and poleward transports. *J. Climate*, **21**, 2313–2325, https://doi.org/10.1175/2007JCLI1936.1.

He, C., A. C. Clement, S. M. Kramer, M. A. Cane, J. M. Klavans, T. M. Fenske, and L. N. Murphy, 2023: Tropical Atlantic multidecadal variability is dominated by external forcing. *Nature*, **622**, 521–527, https://doi.org/10.1038/s41586-023-06489-4.

Heede, U. K., and A. V. Fedorov, 2021: Eastern equatorial Pacific warming delayed by aerosols and thermostat response to CO_2 increase. *Nat. Climate Change*, **11**, 696–703, https://doi.org/10.1038/s41558-021-01101-x.

Horel, J. D., and J. M. Wallace, 1981: Planetary-scale atmospheric phenomena associated with the Southern Oscillation. *Mon. Wea. Rev.*, **109**, 813–829, https://doi.org/10.1175/1520-0493(1981)109<0813:PSAPAW>2.0.CO;2.

Hua, W., A. Dai, and M. Qin, 2018: Contributions of internal variability and external forcing to the recent Pacific decadal variations. *Geophys. Res. Lett.*, **45**, 7084–7092, https://doi.org/10.1029/2018GL079033.

Hurrell, J. W., and Coauthors, 2013: The Community Earth System Model: A framework for collaborative research. *Bull. Amer. Meteor. Soc.*, **94**, 1339–1360, https://doi.org/10.1175/BAMS-D-12-00121.1.

Jenkins, M., and A. Dai, 2021: The impact of sea-ice loss on Arctic climate feedbacks and their role for Arctic amplification. *Geophys. Res. Lett.*, **48**, e2021GL094599, https://doi.org/10.1029/2021GL094599.

Jenkins, M. T., A. Dai, and C. Deser, 2023: Seasonal variations and spatial patterns of Arctic cloud changes in association with sea ice loss during 1950–2019 in ERA5. *J. Climate*, **37**, 735–754, https://doi.org/10.1175/JCLI-D-23-0117.1.

Kapsch, M.-L., R. G. Graversen, M. Tjernström, and R. Bintanja, 2016: The effect of downwelling longwave and shortwave radiation on Arctic summer sea ice. *J. Climate*, **29**, 1143–1159, https://doi.org/10.1175/JCLI-D-15-0238.1.

Kay, J. E., M. M. Holland, and A. Jahn, 2011: Inter-annual to multi-decadal Arctic sea ice extent trends in a warming world. *Geophys. Res. Lett.*, **38**, L15708, https://doi.org/10.1029/2011GL048008.

——, and Coauthors, 2015: The Community Earth System Model (CESM) large ensemble project: A community resource for studying climate change in the presence of internal climate variability. *Bull. Amer. Meteor. Soc.*, **96**, 1333–1349, https://doi.org/10.1175/BAMS-D-13-00255.1.

Kim, Y.-H., S.-K. Min, N. P. Gillett, D. Notz, and E. Malinina, 2023: Observationally-constrained projections of an ice-free Arctic even under a low emission scenario. *Nat. Commun.*, **14**, 3139, https://doi.org/10.1038/s41467-023-38511-8.

Kirchmeier-Young, M. C., F. W. Zwiers, and N. P. Gillett, 2017: Attribution of extreme events in Arctic sea ice extent. *J. Climate*, **30**, 553–571, https://doi.org/10.1175/JCLI-D-16-0412.1.

Kwok, R., 2018: Arctic sea ice thickness, volume, and multiyear ice coverage: Losses and coupled variability (1958–2018). *Environ. Res. Lett.*, **13**, 105005, https://doi.org/10.1088/1748-9326/aae3ec.

Lehner, F., and C. Deser, 2023: Origin, importance, and predictive limits of internal climate variability. *Environ. Res. Climate*, **2**, 023001, https://doi.org/10.1088/2752-5295/accf30.

Lin, P., Z. Yu, J. Lü, M. Ding, A. Hu, and H. Liu, 2019: Two regimes of Atlantic multidecadal oscillation: Cross-basin dependent or Atlantic-intrinsic. *Sci. Bull.*, **64**, 198–204, https://doi.org/10.1016/j.scib.2018.12.027.

Lindsay, R., and A. Schweiger, 2015: Arctic sea ice thickness loss determined using subsurface, aircraft, and satellite observations. *Cryosphere*, **9**, 269–283, https://doi.org/10.5194/tc-9-269-2015.

Liu, W., A. Fedorov, and F. Sévellec, 2019: The mechanisms of the Atlantic meridional overturning circulation slowdown induced by Arctic sea ice decline. *J. Climate*, **32**, 977–996, https://doi.org/10.1175/JCLI-D-18-0231.1.

Liu, Z., and Coauthors, 2021: Acceleration of western Arctic sea ice loss linked to the Pacific North American pattern. *Nat. Commun.*, **12**, 1519, https://doi.org/10.1038/s41467-021-21830-z.

Livina, V. N., and T. M. Lenton, 2013: A recent tipping point in the Arctic sea-ice cover: Abrupt and persistent increase in the seasonal cycle since 2007. *Cryosphere*, **7**, 275–286, https://doi.org/10.5194/tc-7-275-2013.

Mahajan, S., R. Zhang, and T. L. Delworth, 2011: Impact of the Atlantic meridional overturning circulation (AMOC) on Arctic surface air temperature and sea ice variability. *J. Climate*, **24**, 6573–6581, https://doi.org/10.1175/2011JCLI4002.1.

Massonnet, F., T. Fichefet, H. Goosse, C. M. Bitz, G. Philippon-Berthier, M. M. Holland, and P.-Y. Barriat, 2012: Constraining projections of summer Arctic sea ice. *Cryosphere*, **6**, 1383–1394, https://doi.org/10.5194/tc-6-1383-2012.

Meehl, G. A., C. T. Y. Chung, J. M. Arblaster, M. M. Holland, and C. M. Bitz, 2018: Tropical decadal variability and the rate of Arctic sea ice decrease. *Geophys. Res. Lett.*, **45**, 11 326–11 333, https://doi.org/10.1029/2018GL079989.

——, and Coauthors, 2021: Atlantic and Pacific tropics connected by mutually interactive decadal-timescale processes. *Nat. Geosci.*, **14**, 36–42, https://doi.org/10.1038/s41561-020-00669-x.

Min, S.-K., X. Zhang, F. W. Zwiers, and T. Agnew, 2008: Human influence on Arctic sea ice detectable from early 1990s onwards. *Geophys. Res. Lett.*, **35**, L21701, https://doi.org/10.1029/2008GL035725.

Morrison, A. L., J. E. Kay, W. R. Frey, H. Chepfer, and R. Guzman, 2019: Cloud response to Arctic sea ice loss and implications for future feedback in the CESM1 climate model. *J. Geophys. Res. Atmos.*, **124**, 1003–1020, https://doi.org/10.1029/2018JD029142.

Moss, R. H., and Coauthors, 2010: The next generation of scenarios for climate change research and assessment. *Nature*, **463**, 747–756, https://doi.org/10.1038/nature08823.

Mueller, B. L., N. P. Gillett, A. H. Monahan, and F. W. Zwiers, 2018: Attribution of Arctic sea ice decline from 1953 to 2012 to influences from natural, greenhouse gas, and anthropogenic aerosol forcing. *J. Climate*, **31**, 7771–7787, https://doi.org/10.1175/JCLI-D-17-0552.1.

Murphy, L. N., J. M. Klavans, A. C. Clement, and M. A. Cane, 2021: Investigating the roles of external forcing and ocean circulation on the Atlantic multidecadal SST variability in a large ensemble climate model hierarchy. *J. Climate*, **34**, 4835–4849, https://doi.org/10.1175/JCLI-D-20-0167.1.

Notz, D., and J. Marotzke, 2012: Observations reveal external driver for Arctic sea-ice retreat. *Geophys. Res. Lett.*, **39**, L08502, https://doi.org/10.1029/2012GL051094.

——, and J. Stroeve, 2016: Observed Arctic sea-ice loss directly follows anthropogenic CO_2 emission. *Science*, **354**, 747–750, https://doi.org/10.1126/science.aag2345.

——, and SIMIP Community, 2020: Arctic sea ice in CMIP6. *Geophys. Res. Lett.*, **47**, e2019GL086749, https://doi.org/10.1029/2019GL086749.

Onarheim, I. H., T. Eldevik, L. H. Smedsrud, and J. C. Stroeve, 2018: Seasonal and regional manifestation of Arctic sea ice loss. *J. Climate*, **31**, 4917–4932, https://doi.org/10.1175/JCLI-D-17-0427.1.

Parkinson, C. L., 2014: Global sea ice coverage from satellite data: Annual cycle and 35-yr trends. *J. Climate*, **27**, 9377–9382, https://doi.org/10.1175/JCLI-D-14-00605.1.

Pinto, J. O., A. Alam, J. A. Maslanik, J. A. Curry, and R. S. Stone, 2003: Surface characteristics and atmospheric footprint of springtime Arctic leads at SHEBA. *J. Geophys. Res.*, **108**, 8051, https://doi.org/10.1029/2000JC000473.

Polyakov, I. V., J. E. Walsh, and R. Kwok, 2012: Recent changes of Arctic multiyear sea ice coverage and the likely causes. *Bull. Amer. Meteor. Soc.*, **93**, 145–151, https://doi.org/10.1175/BAMS-D-11-00070.1.

Qin, M., A. Dai, and W. Hua, 2020a: Quantifying contributions of internal variability and external forcing to Atlantic multidecadal variability since 1870. *Geophys. Res. Lett.*, **47**, e2020GL089504, https://doi.org/10.1029/2020GL089504.

——, ——, and ——, 2020b: Aerosol-forced multidecadal variations across all ocean basins in models and observations since 1920. *Sci. Adv.*, **6**, eabb0425, https://doi.org/10.1126/sciadv.abb0425.

Rayner, N. A., D. E. Parker, E. B. Horton, C. K. Folland, L. V. Alexander, D. P. Rowell, E. C. Kent, and A. Kaplan, 2003: Global analyses of sea surface temperature, sea ice, and night marine air temperature since the late nineteenth century. *J. Geophys. Res.*, **108**, 4407, https://doi.org/10.1029/2002JD002670.

Roberts, C. D., M. D. Palmer, R. P. Allan, D. G. Desbruyeres, P. Hyder, C. Liu, and D. Smith, 2017: Surface flux and ocean heat transport convergence contributions to seasonal and interannual variations of ocean heat content. *J. Geophys. Res. Oceans*, **122**, 726–744, https://doi.org/10.1002/2016JC012278.

Ruprich-Robert, Y., R. Msadek, F. Castruccio, S. Yeager, T. Delworth, and G. Danabasoglu, 2017: Assessing the climate impacts of the observed Atlantic multidecadal variability using the GFDL CM2.1 and NCAR CESM1 global coupled models. *J. Climate*, **30**, 2785–2810, https://doi.org/10.1175/JCLI-D-16-0127.1.

Scaife, A. A., and D. Smith, 2018: A signal-to-noise paradox in climate science. *npj Climate Atmos. Sci.*, **1**, 28, https://doi.org/10.1038/s41612-018-0038-4.

Schweiger, A. J., K. R. Wood, and J. Zhang, 2019: Arctic sea ice volume variability over 1901–2010: A model-based reconstruction. *J. Climate*, **32**, 4731–4752, https://doi.org/10.1175/JCLI-D-19-0008.1.

Screen, J. A., and I. Simmonds, 2010: The central role of diminishing sea ice in recent Arctic temperature amplification. *Nature*, **464**, 1334–1337, https://doi.org/10.1038/nature09051.

——, and J. A. Francis, 2016: Contribution of sea-ice loss to Arctic amplification is regulated by Pacific Ocean decadal variability. *Nat. Climate Change*, **6**, 856–860, https://doi.org/10.1038/nclimate3011.

——, and C. Deser, 2019: Pacific Ocean variability influences the time of emergence of a seasonally ice-free Arctic Ocean. *Geophys. Res. Lett.*, **46**, 2222–2231, https://doi.org/10.1029/2018GL081393.

Serreze, M. C., M. M. Holland, and J. Stroeve, 2007: Perspectives on the Arctic's shrinking sea-ice cover. *Science*, **315**, 1533–1536, https://doi.org/10.1126/science.1139426.

Si, D., A. Hu, D. Jiang, and X. Lang, 2023: Atmospheric teleconnection associated with the Atlantic multidecadal variability in summer: Assessment of the CESM1 model. *Climate Dyn.*, **60**, 1043–1060, https://doi.org/10.1007/s00382-022-06331-z.

Singh, H. A., P. J. Rasch, and B. E. J. Rose, 2017: Increased ocean heat convergence into the high latitudes with CO_2 doubling enhances polar-amplified warming. *Geophys. Res. Lett.*, **44**, 10 583–10 591, https://doi.org/10.1002/2017GL074561.

Smith, D. M., and Coauthors, 2016: Role of volcanic and anthropogenic aerosols in the recent global surface warming slowdown. *Nat. Climate Change*, **6**, 936–940, https://doi.org/10.1038/nclimate3058.

——, and Coauthors, 2019: Robust skill of decadal climate predictions. *npj Climate Atmos. Sci.*, **2**, 13, https://doi.org/10.1038/s41612-019-0071-y.

——, and Coauthors, 2020: North Atlantic climate far more predictable than models imply. *Nature*, **583**, 796–800, https://doi.org/10.1038/s41586-020-2525-0.

Smith, T. M., R. W. Reynolds, T. C. Peterson, and J. Lawrimore, 2008: Improvements to NOAA's historical merged land–ocean surface temperature analysis (1880–2006). *J. Climate*, **21**, 2283–2296, https://doi.org/10.1175/2007JCLI2100.1.

Song, M., L. Wei, and Z. Wang, 2016: Quantifying the contribution of natural variability to September Arctic sea ice decline. *Acta Oceanol. Sin.*, **35**, 49–53, https://doi.org/10.1007/s13131-016-0854-5.

Stroeve, J., M. M. Holland, W. Meier, T. Scambos, and M. Serreze, 2007: Arctic sea ice decline: Faster than forecast. *Geophys. Res. Lett.*, **34**, L09501, https://doi.org/10.1029/2007GL029703.

Stroeve, J. C., V. Kattsov, A. Barrett, M. Serreze, T. Pavlova, M. Holland, and W. N. Meier, 2012: Trends in Arctic sea ice extent from CMIP5, CMIP3 and observations. *Geophys. Res. Lett.*, **39**, L16502, https://doi.org/10.1029/2012GL052676.

Svendsen, L., N. Keenlyside, M. Muilwijk, I. Bethke, N.-E. Omrani, and Y. Gao, 2021: Pacific contribution to decadal surface temperature trends in the Arctic during the twentieth century. *Climate Dyn.*, **57**, 3223–3243, https://doi.org/10.1007/s00382-021-05868-9.

Swart, N. C., J. C. Fyfe, E. Hawkins, J. E. Kay, and A. Jahn, 2015: Influence of internal variability on Arctic sea-ice trends. *Nat. Climate Change*, **5**, 86–89, https://doi.org/10.1038/nclimate2483.

Topál, D., and Q. Ding, 2023: Atmospheric circulation-constrained model sensitivity recalibrates Arctic climate projections. *Nat. Climate Change*, **13**, 710–718, https://doi.org/10.1038/s41558-023-01698-1.

Trenberth, K. E., 1997: Using atmospheric budgets as a constraint on surface fluxes. *J. Climate*, **10**, 2796–2809, https://doi.org/10.1175/1520-0442(1997)010<2796:UABAAC>2.0.CO;2.

Vihma, T., P. Tisler, and P. Uotila, 2012: Atmospheric forcing on the drift of Arctic sea ice in 1989–2009. *Geophys. Res. Lett.*, **39**, L02501, https://doi.org/10.1029/2011GL050118.

Walsh, J. E., F. Fetterer, J. Scott Stewart, and W. L. Chapman, 2017: A database for depicting Arctic sea ice variations back to 1850. *Geogr. Rev.*, **107**, 89–107, https://doi.org/10.1111/j.1931-0846.2016.12195.x.

Wang, M., and J. E. Overland, 2009: A sea ice free summer Arctic within 30 years? *Geophys. Res. Lett.*, **36**, L07502, https://doi.org/10.1029/2009GL037820.

——, and ——, 2012: A sea ice free summer Arctic within 30 years: An update from CMIP5 models. *Geophys. Res. Lett.*, **39**, L18501, https://doi.org/10.1029/2012GL052868.

Wang, T., and J.-P. Miao, 2017: Twentieth-century Pacific decadal oscillation simulated by CMIP5 coupled models. *Atmos. Ocean. Sci. Lett.*, **11**, 94–101, https://doi.org/10.1080/16742834.2017.1381548.

Wang, Z., Y. Li, B. Liu, and J. Liu, 2015: Global climate internal variability in a 2000-year control simulation with Community Earth System Model (CESM). *Chin. Geogr. Sci.*, **25**, 263–273, https://doi.org/10.1007/s11769-015-0754-1.

Wernli, H., and L. Papritz, 2018: Role of polar anticyclones and mid-latitude cyclones for Arctic summertime sea-ice melting. *Nat. Geosci.*, **11**, 108–113, https://doi.org/10.1038/s41561-017-0041-0.

Wills, R. C. J., Y. Dong, C. Proistosecu, K. C. Armour, and D. S. Battisti, 2022: Systematic climate model biases in the large-scale patterns of recent sea-surface temperature and sea-level pressure change. *Geophys. Res. Lett.*, **49**, e2022GL100011, https://doi.org/10.1029/2022GL100011.

Woodgate, R. A., T. Weingartner, and R. Lindsay, 2010: The 2007 Bering Strait oceanic heat flux and anomalous Arctic sea-ice retreat. *Geophys. Res. Lett.*, **37**, L01602, https://doi.org/10.1029/2009GL041621.

Yang, D., J. M. Arblaster, G. A. Meehl, M. H. England, E.-P. Lim, S. Bates, and N. Rosenbloom, 2020: Role of tropical variability in driving decadal shifts in the Southern Hemisphere summertime eddy-driven jet. *J. Climate*, **33**, 5445–5463, https://doi.org/10.1175/JCLI-D-19-0604.1.

Yang, X.-Y., G. Wang, and N. Keenlyside, 2020: The Arctic sea ice extent change connected to Pacific decadal variability. *Cryosphere*, **14**, 693–708, https://doi.org/10.5194/tc-14-693-2020.

Yu, L., S. Zhong, J. A. Winkler, M. Zhou, D. H. Lenschow, B. Li, X. Wang, and Q. Yang, 2017: Possible connections of the opposite trends in Arctic and Antarctic sea-ice cover. *Sci. Rep.*, **7**, 45804, https://doi.org/10.1038/srep45804.

Zhang, P., G. Chen, M. Ting, L. R. Leung, B. Guan, and L. Li, 2023: More frequent atmospheric rivers slow the seasonal recovery of Arctic sea ice. *Nat. Climate Change*, **13**, 266–273, https://doi.org/10.1038/s41558-023-01599-3.

Zhang, R., 2015: Mechanisms for low-frequency variability of summer Arctic sea ice extent. *Proc. Natl. Acad. Sci. USA*, **112**, 4570–4575, https://doi.org/10.1073/pnas.1422296112.

——, R. Sutton, G. Danabasoglu, Y.-O. Kwon, R. Marsh, S. G. Yeager, D. E. Amrhein, and C. M. Little, 2019: A review of the role of the Atlantic meridional overturning circulation in Atlantic multidecadal variability and associated climate impacts. *Rev. Geophys.*, **57**, 316–375, https://doi.org/10.1029/2019RG000644.